Nano Research

Open Access

Research Article

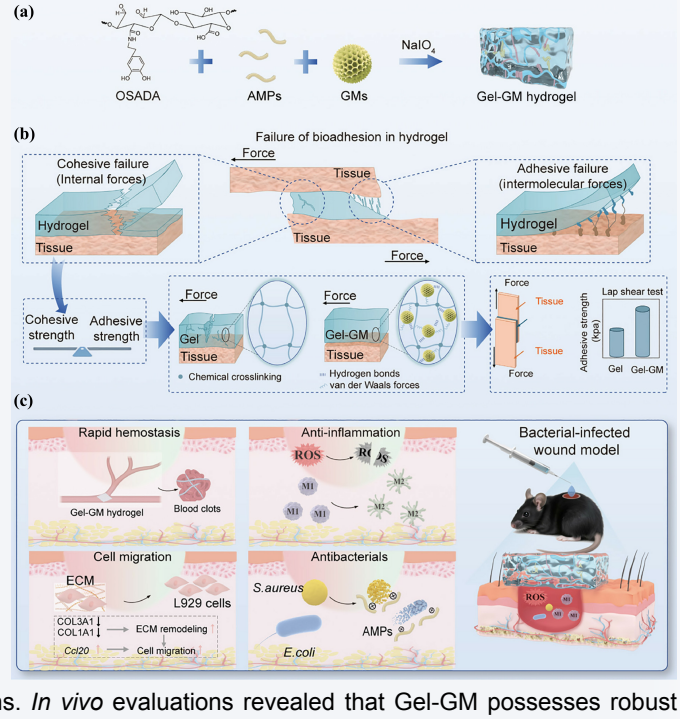
Cohesion-adhesion balanced microsphere-reinforced hydrogel promotes bacterial-infected wound healing by modulating the inflammatory microenvironment

Min Li[1,2,§], He Zhang[2,3,§], Zhuqing Wan[1,2], Min Yu[1,2], Xiaodong Guo[1,2], Liyuan Chen[2,3], Xinjia Cai[2,3], Zeyu Wang[4], Lifang Feng[4], Longwei Lv[1,2], Yunsong Liu[1,2], Dandan Xia[2,5] ✉, Yan Liu[2,3] ✉, and Yongsheng Zhou[1,2] ✉

[1] *Department of Prosthodontics, Peking University School and Hospital of Stomatology, Beijing 100081, China*
[2] *Beijing Key Laboratory for Intelligent Biomanufacturing and Regeneration of Craniofacial Tissues & National Center for Stomatology & National Clinical Research Center for Oral Diseases & National Engineering Research Center of Oral Biomaterials and Digital Medical Devices & Beijing Key Laboratory of Digital Stomatology & NHC Key Laboratory of Digital Stomatology & NMPA Key Laboratory for Dental Materials, Beijing 100081, China*
[3] *Central Laboratory, Department of Orthodontics, Peking University School and Hospital of Stomatology, Beijing Advanced Center of Cellular Homeostasis and Aging-Related Diseases & State Key Laboratory of Natural and Biomimetic Drugs, Beijing 100081, China*
[4] *College of Stomatology, North China University of Science and Technology, Tangshan 063210, China*
[5] *Department of Dental Materials, Peking University School and Hospital of Stomatology, Beijing 100081, China*
§ *Min Li and He Zhang contributed equally to this work.*

Cite this article: *Nano Research*, **2026**, *19*, 94908900. https://doi.org/10.26599/NR.2026.94908900

ABSTRACT: Chronic infected wounds experience delayed healing due to persistent bacterial colonization, excessive accumulation of reactive oxygen species (ROS), and prolonged inflammation. Although adhesive hydrogels are promising as wound dressings, challenges in achieving strong tissue adhesion coupled with adequate internal cohesion have hindered their clinical application. Here, we developed a multifunctional adhesive hydrogel designed around a cohesion–adhesion balance strategy for infected wound treatment. Specifically, we synthesized a gelatin microsphere-reinforced adhesive hydrogel (Gel-GM) by embedding gelatin microspheres (GMs) and the antimicrobial peptide LL-37 into a dopamine-grafted alginate network. Incorporation of GMs strengthened the hydrogel network through increased intermolecular interactions, enhancing cohesive strength while preserving sufficient exposed catechol groups to ensure interfacial adhesion. *In vitro* studies demonstrated that Gel-GM significantly improves ROS scavenging, promotes anti-inflammatory M2 macrophage polarization, and enhances fibroblast proliferation and migration. Additionally, LL-37 confers potent antibacterial activity by disrupting bacterial membranes via electrostatic interactions. *In vivo* evaluations revealed that Gel-GM possesses robust antibacterial and anti-inflammatory properties, effectively accelerating infected wound healing. Collectively, this study emphasizes the potential of employing a cohesion–adhesion balance approach to engineer multifunctional adhesive hydrogels for managing infected wounds.



KEYWORDS: adhesive hydrogel, inflammatory microenvironment, adhesion, cohesion, bacterial-infected wound healing

Received: March 13, 2026; **Revised:** May 22, 2026; **Accepted:** May 29, 2026

✉Address correspondence to Dandan Xia, dandanxia@pku.edu.cn; Yan Liu, orthoyan@bjmu.edu.cn; Yongsheng Zhou, kqzhouysh@hsc.pku.edu.cn

1 Introduction

With global population aging and the rising incidence of obesity and systemic diseases, chronic wounds, including vascular ulcers, pressure injuries, and diabetic foot ulcers, are becoming increasingly common. These wounds are highly susceptible to infections and complications, significantly burdening global healthcare systems and economies [1]. In acute wounds, skin barrier disruption initiates a healing cascade involving hemostasis, inflammation, proliferation, and remodeling. This cascade triggers the release of various growth factors, promoting angiogenesis and extracellular matrix (ECM) component synthesis, particularly collagen, to facilitate tissue regeneration [2, 3]. In contrast, chronic wounds exhibit repeated bacterial infections and prolonged inflammatory responses, resulting in delayed or impaired healing. Infection and associated complications severely impede wound repair, as initial microbial colonization can influence cellular responses essential to healing [4]. Consequently, mitigating microbial infection and enhancing wound healing remain critical goals in managing chronic infected wounds. Typically, chronic wound microenvironments are characterized by sustained inflammation and reactive oxygen species (ROS) accumulation. The complexity of such wounds necessitates novel therapeutic strategies capable of simultaneously exerting anti-inflammatory and antibacterial functions [5]. Currently, adhesive hydrogel dressings exhibit limitations regarding dynamic adhesive durability, mechanical strength, and active microenvironment modulation [6–8]. In recent years, mussel-inspired catechol-based adhesive hydrogels have attracted significant attention for their applications in burn wounds [9], infected wounds [10] and diabetic wounds [11], due to their anti-inflammatory, antioxidant, adhesive properties, and favorable outcomes in tissue regeneration. Dopamine (DA), a tyrosine derivative present in mussel adhesive proteins, is frequently employed to fabricate catechol-based composite hydrogels, leveraging its free reactive amino group [12]. The catechol moiety effectively scavenges ROS, modulates macrophage polarization, enhances wound microenvironments, and controls inflammation, in addition to providing excellent biocompatibility and antioxidant capabilities. Furthermore, incorporated catechol structures impart adhesiveness to hydrogel dressings, facilitating hemostasis and physical wound sealing [13, 14].

The adhesion performance of hydrogel-based wound dressings is governed by two interacting factors: interfacial adhesion, which arises from molecular interactions between functional groups (such as catechols) and the tissue surface, and cohesive strength, which depends on the internal mechanical integrity of the hydrogel network itself [15, 16]. These forces cannot be tuned independently. When cohesive strength is inadequate, the bulk hydrogel fractures before interfacial bonds can sustain loads, resulting in structural failure; conversely, excessive cohesion stiffens the network and restricts the conformational flexibility of adhesive groups, thereby reducing their effective contact with the substrate and diminishing interfacial adhesion [15, 17]. Thus, achieving an intentional balance between these forces, known as the "cohesion–adhesion balance", is crucial for optimizing the adhesive performance of catechol-based hydrogels. Guided by this principle, the current study employed porous gelatin microspheres (GMs) within the catechol-based hydrogel network as a targeted strategy for enhancing cohesion. Incorporating GMs reinforced the network through strengthened intermolecular interactions, resulting in a dynamic and interconnected three-dimensional structure that elevated bulk cohesive strength to an optimal range [18, 19]. Consequently, this allowed greater exposure of catechol groups at the hydrogel surface, enhancing their interaction with the wound bed without compromising multifunctionality. Additionally, the porous structure of GMs served as a cell-compatible scaffold, promoting cell adhesion and accelerating tissue regeneration.

In this study, we successfully developed a cohesive-adhesive balanced hydrogel reinforced by porous GMs (Gel-GM), incorporating GMs and the antimicrobial peptide (AMP) LL-37 into a dopamine-modified alginate hydrogel (Scheme 1). The human-derived AMP LL-37, recognized for facilitating pressure ulcer healing, primarily provided antibacterial activity within this hydrogel system. This hydrogel demonstrated robust adhesiveness and self-healing properties, enabling it to conform to wounds of varying shapes for effective treatment of infected wounds. The introduction of GMs enhanced intermolecular interactions, primarily electrostatic forces, thereby reinforcing the hydrogel's adhesive performance. Simultaneously, the increased hydrogen bonding imparted notable self-healing capabilities. Additionally, catechol groups effectively scavenged ROS and promoted macrophage polarization toward the anti-inflammatory M2 phenotype, thereby improving the wound microenvironment and mitigating excessive inflammation. *In vivo* experiments indicated that the Gel-GM hydrogel exhibited pronounced antibacterial and anti-inflammatory effects within 7–10 days post-application. During this period, Gel-GM effectively promoted fibroblast migration through modulation of ECM remodeling, significantly accelerating infected wound healing. By day 14, wounds treated with Gel-GM had completely healed, with regeneration of skin accessory structures.

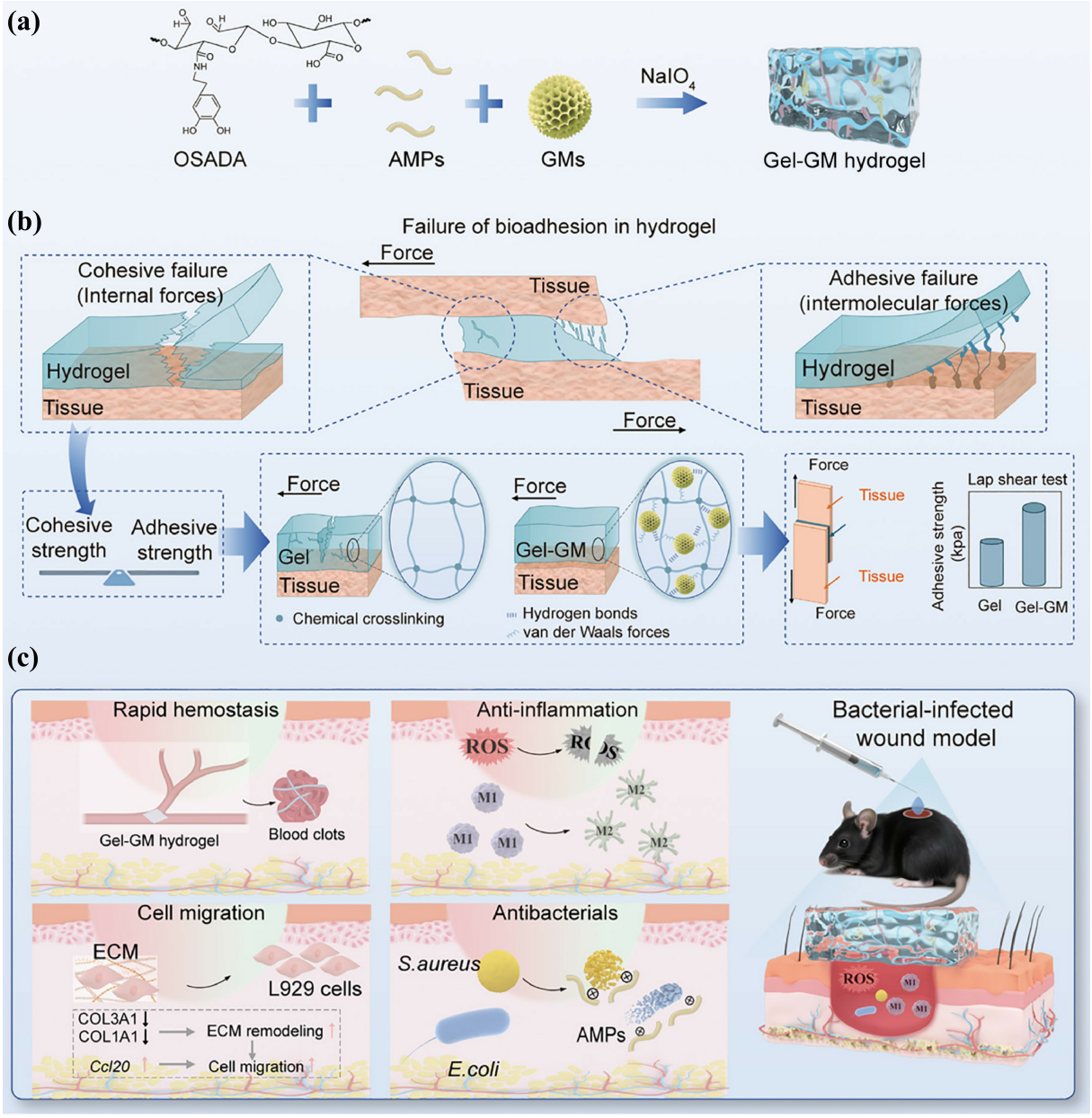
In summary, the Gel-GM multifunctional adhesive hydrogel exerted temporally regulated functions throughout the wound healing process: promoting cellular migration alongside anti-inflammatory and antibacterial effects during the initial stages and accelerating healing via enhanced collagen deposition during the subsequent proliferation and remodeling stages. Thus, this adhesive hydrogel not only markedly improved wound repair and regeneration but also overcame limitations associated with traditional wound dressings, such as insufficient bactericidal activity and poor dynamic adaptability. Accordingly, the Gel-GM hydrogel represents a promising therapeutic approach for managing chronic infected wounds.

2 Results and discussion

2.1 Preparation and characterization of Gel-GM hydrogels

A multifunctional hydrogel exhibiting adhesive, antioxidant, and antibacterial activities was fabricated, and its rheological properties, ROS-scavenging ability, adhesive performance, and antibacterial effects were evaluated to promote infected wound healing (Scheme 1).

Sodium alginate (Alg), a natural biopolymer derived from brown algae, demonstrates significant potential as a wound dressing for skin repair due to its biocompatibility and structural similarity to the ECM [20]. Because Alg lacks corresponding degradation enzymes *in vivo*, it exhibits limited degradability. However, oxidation decreases its molecular weight, thus enhancing its degradation rate and minimizing secondary injuries caused by



Scheme 1 Schematic representation illustrating (a) the fabrication of porous Gel-GM, (b) its strong adhesion mechanism, and (c) its role in promoting infected wound healing.

frequent dressing replacements [21]. Oxidized sodium alginate (OSA), a derivative of Alg, possesses excellent moisture retention properties and an adjustable degradation rate, making it particularly suitable for wound healing [22]. To impart adhesive capabilities, DA was grafted onto OSA. Specifically, Alg was first oxidized with sodium periodate ($NaIO_4$) to produce OSA, followed by grafting DA onto OSA via 1-ethyl-3-(3-dimethylaminopropyl)carbodiimide/*N*-hydroxysuccinimide (EDC/NHS) amidation, yielding dopamine-modified oxidized sodium alginate (OSADA) (Fig. 1(a)). Fourier transform infrared (FTIR) spectroscopy analysis of OSADA showed a characteristic absorption peak at approximately 1280 cm^{-1}, indicative of DA incorporation (Fig. 1(b)) [23]. Additionally, the ^1H nuclear magnetic resonance (NMR) spectrum of OSADA exhibited a distinct aldehyde proton signal near 5.0 ppm, along with aromatic proton signals at 6.5–7.0 ppm corresponding to benzene ring protons of DA [24], confirming successful DA grafting onto OSA (Fig. 1(c)). Furthermore, the characteristic catechol peak of DA at 280 nm in the ultraviolet–visible (UV–Vis) spectrum further verified the successful synthesis of OSADA (Fig. 1(d)). Gel and Gel-GM hydrogels were subsequently prepared by oxidatively crosslinking OSADA with $NaIO_4$ solution, with specific formulations listed in Table S1 in the Electronic Supplementary Material (ESM). The Gel-GM hydrogel incorporated AMPs and porous GMs at room temperature (Figs. 1(e) and 1(f)). The GMs provided a supportive scaffold for fibroblast growth, facilitating cell adhesion and proliferation (Fig. S1 in the ESM). The resulting Gel-GM hydrogel exhibited intrinsic adhesiveness and notable stretchability, enabling adaptive conformation to skin wounds and rendering it suitable for treating wounds of diverse shapes (Fig. 1(g)). Scanning electron microscopy (SEM) revealed the porous microstructure of the GM-reinforced hydrogel (Gel-GM), clearly displaying the integration and interactive network formed

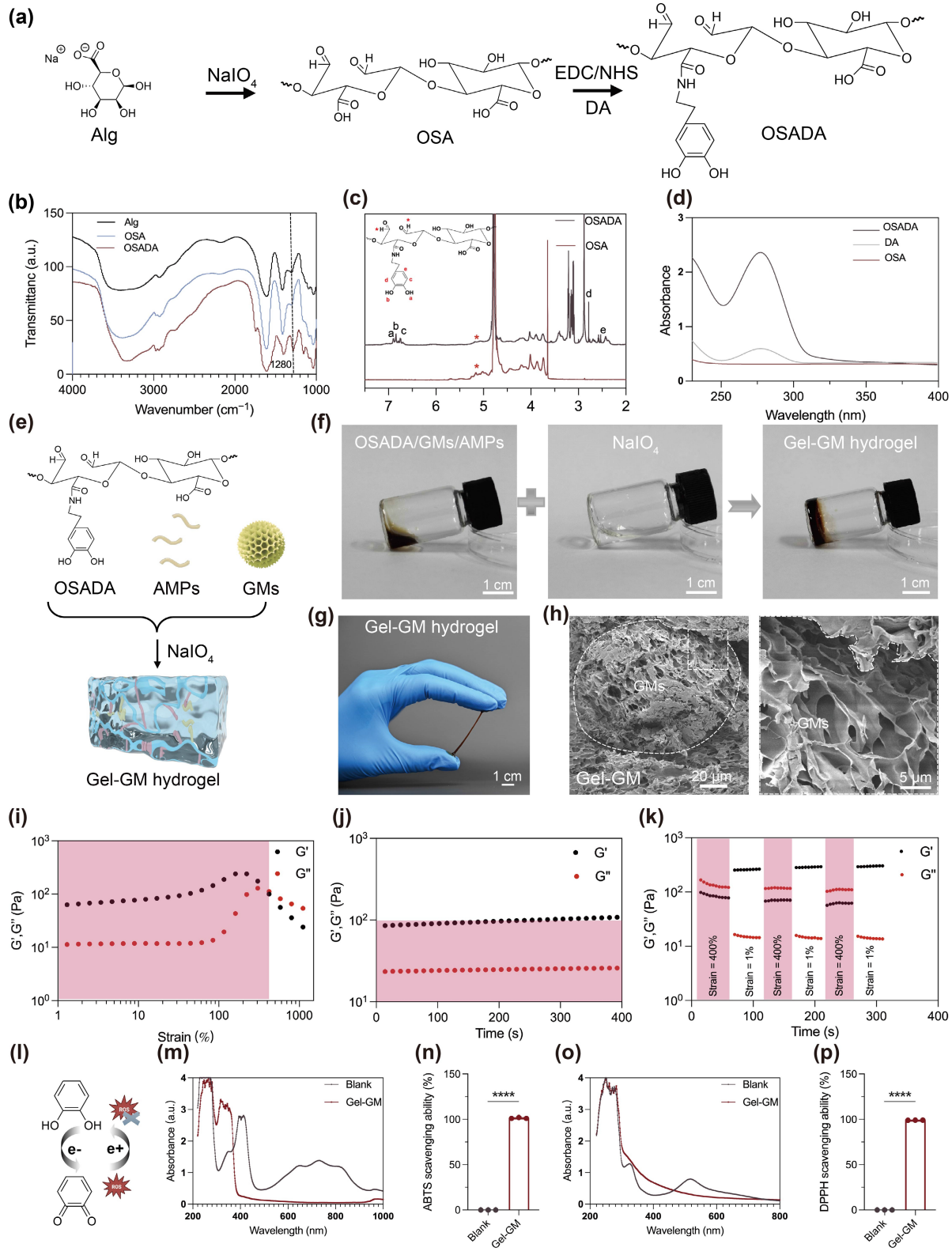


Figure 1 Preparation, characterization, and antioxidant properties of Gel-GM hydrogels. (a) Synthetic route and chemical structure of OSADA. (b) FTIR spectra, (c) ^{1}H NMR spectra, and (d) UV–Vis spectra. (e) and (f) Schematics illustrating the sol-gel transition from a precursor solution to the Gel-GM hydrogel. (g) Photographs demonstrating the adhesive property and remarkable stretchability of the Gel-GM hydrogel. (h) SEM images of Gel-GM hydrogel. Rheological characterization of Gel-GM hydrogel, including (i) strain sweep, (j) time sweep, and (k) alternating strain tests. (l) Schematic illustration of the ROS-scavenging mechanism. Antioxidant activity assessments: $ABTS^{+}$ radical scavenging represented by (m) UV–Vis absorption spectra and (n) quantitative scavenging rates; DPPH· radical scavenging represented by (o) UV–Vis absorption spectra and (p) quantitative scavenging rates (n = 3). Data represent mean ± standard deviation (SD); $^{*}P < 0.05$, $^{**}P < 0.01$, $^{***}P < 0.001$, $^{****}P < 0.0001$ (Student's t-test).

between GMs and the hydrogel matrix (Fig. 1(h)). Compared with Gel alone, the addition of GMs resulted in a more porous and interconnected internal microstructure within Gel-GM hydrogels (Fig. S3 in the ESM).

Given the fixed elastic strength of skin, the design of biomimetic hydrogels adaptable to various conditions is essential. Rheological analyses were conducted to characterize hydrogel properties. A material exhibits a solid-like state when the storage modulus (G') surpasses the loss modulus (G''), whereas a liquid-like state occurs when the opposite is true. Initially, strain sweep tests determined the critical strain threshold. For Gel-GM, G'' surpassed G' at approximately 400% strain, indicating total structural disruption (Fig. 1(i)). Time sweep tests demonstrated that Gel-GM maintained structural stability under a constant frequency of 1 Hz (Fig. 1(j)). Subsequent alternating strain tests evaluated self-healing properties. At 400% strain, the hydrogel network was disrupted; however, upon reducing the strain to 1%, the network demonstrated structural recovery (Fig. 1(k)). These experimental outcomes confirmed the self-healing ability of Gel-GM [25]. Concurrently, rheological results revealed that GM incorporation significantly enhanced the cohesive strength relative to Gel, with Gel-GM exhibiting the highest G' value (Fig. S3(d) in the ESM).

Catechol groups have excellent antioxidant capabilities, exerted via their conversion to quinones through electron and proton transfer (Fig. 1(l)) [26]. The antioxidant performance of Gel-GM hydrogel was assessed by measuring its radical-scavenging ability against $ABTS^{+}$ and DPPH· radicals. Upon addition of Gel-GM, the 2,2'-azino-bis(3-ethylbenzothiazoline-6-sulfonic acid) (ABTS) solution changed from blue to pale yellow, and the deep purple 2,2-diphenyl-1-picrylhydrazyl (DPPH) solution became light yellow. Absorption spectra showed the disappearance of characteristic peaks for $ABTS^{+}$ at 734 nm (Fig. 1(m)) and DPPH· at 517 nm (Fig. 1(o)). Optical density (OD) measurements revealed radical scavenging rates of 100% for both $ABTS^{+}$ (Fig. 1(n)) and DPPH· (Fig. 1(p)), confirming the hydrogel's outstanding antioxidant capacity. Furthermore, Gel-GM maintained antioxidant activity comparable to that of Gel hydrogel (Fig. S3(e) in the ESM). Owing to its optimal mechanical integrity and bioactivity, Gel-GM was selected for further experiments.

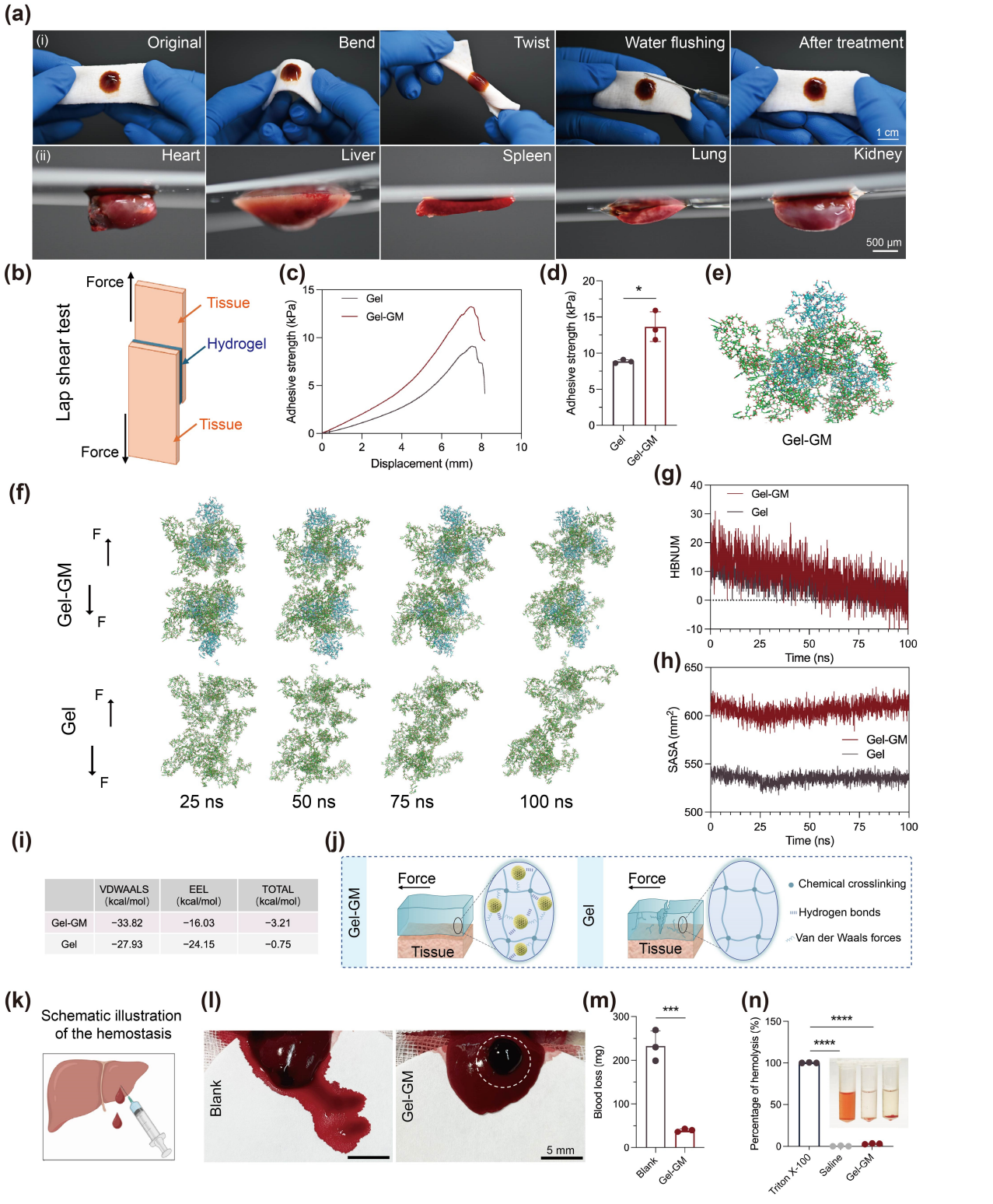
2.2 Adhesive properties, molecular dynamics (MD) simulations, and hemostasis performance of Gel-GM hydrogels

Strong adhesive properties are critical for effective wound treatment. To enhance adhesion by improving cohesive strength [17], GMs were integrated into the hydrogel matrix. The adhesive performance of Gel-GM was first evaluated *in vitro*. Gel-GM adhered firmly to porcine skin under bending, twisting, and wet conditions, and showed strong adhesion to various mouse tissues (heart, liver, spleen, lungs, and kidneys) (Fig. 2(a)). Adhesion strength of Gel-GM to porcine skin was quantified by lap shear testing (Fig. 2(b)). Comparison between Gel-GM (containing GMs) and GM-free Gel demonstrated that Gel-GM exhibited significantly higher peak strength (13.3 kPa) compared to Gel (8.85 kPa) (Figs. 2(c) and 2(d)). These findings indicated enhanced adhesive strength due to GM incorporation. The shear adhesion strength of Gel-GM (13.3 kPa) substantially surpassed commercial fibrin glue (1–7 kPa) [27], underscoring its suitability for mechanical demands in wound dressings, while also providing favorable biocompatibility and ease of use.

To elucidate the mechanism underlying this enhanced adhesion, MD simulations were employed. This method visually captures molecular alterations, enabling predictions of intermolecular interactions and microstructural transformations [28]. Initially, a hydrogel network model was constructed (Fig. 2(e)) and subjected to tensile simulations. Structural changes were documented at intervals of 25, 50, 75, and 100 ns. During stretching, the Gel group underwent more significant deformation, whereas the Gel-GM group showed less deformation, indicating stronger internal molecular interactions (Fig. 2(f)) and thus greater resistance to external forces. Differences in SASA were analyzed. SASA trends reflect structural alterations and indicate the degree of hydrophobic surface encapsulation. Higher SASA values represent more exposed surface areas and fewer encapsulated hydrophobic regions, while lower values correspond to compact structures with greater encapsulation. As stretching progressed, the Gel group became structurally looser, as evidenced by increased SASA. In comparison, the Gel-GM group displayed a smaller change in SASA (Fig. 2(h)). To further illustrate this trend, hydrogen bonds within each group were quantified. The Gel-GM hydrogel showed a slightly higher number of hydrogen bonds than the Gel group, though a reduction in hydrogen bonds occurred in both groups during stretching. By 100 ns, hydrogen bonds within the Gel group had nearly disappeared (Fig. 2(g)).

Finally, intermolecular interaction strength was assessed by analyzing binding free energy. Both groups exhibited negative total free energy values, confirming attractive intermolecular forces. Notably, the Gel-GM group had lower (more negative) values, indicative of stronger intermolecular forces (Fig. 2(i)). These results clearly demonstrate that Gel-GM's enhanced adhesion is due to significantly increased cohesive strength.

Related studies [29] support the pivotal role of hydrogels' enhanced mechanical properties in promoting tissue adhesion. The molecular simulation data presented here unequivocally demonstrate that the superior cohesive strength of Gel-GM arises from its more compact structure (as evidenced by the smaller increase in SASA), stronger and more stable hydrogen-bond network, and stronger intermolecular interactions (indicated by the more negative binding free energy). The enhanced intermolecular forces thus enable the material to exhibit greater shear strength (Fig. 2(j)). Cohesive strength, a fundamental mechanical property, describes a material's capacity to resist internal failure. It is established that, with a constant number of adhesive groups on the hydrogel surface, enhancing hydrogel cohesive strength effectively improves adhesion [15]. Therefore, cohesive strength also influences adhesion force magnitude. Hydrogels with superior adhesive properties have significant potential for use in hemostatic applications [30]. An ideal hemostatic adhesive is characterized by rapid gelation, strong adhesion, and excellent biocompatibility. Consequently, Gel-GM hydrogel's exceptional tissue adhesion indicates its suitability for hemostatic applications. Hemostatic efficacy was quantitatively evaluated using a rat liver injury model (Fig. 2(k)). After liver puncture, the hydrogel was promptly applied to the wound, achieving sealing and hemostasis within seconds (Fig. 2(l)). The untreated group experienced substantial blood loss (232.7 mg), significantly greater than the Gel-GM group (39.67 mg) (Fig. 2(m)). In addition, the Gel-GM hydrogel exhibited excellent hemocompatibility in the hemolysis assay, exhibiting a hemolysis rate less than 5% (Fig. 2(n)).



	VDWAALS (kcal/mol)	EEL (kcal/mol)	TOTAL (kcal/mol)
Gel-GM	−33.82	−16.03	−3.21
Gel	−27.93	−24.15	−0.75

Figure 2 Adhesion strength, MD simulation, and hemostasis performance of hydrogels. (a) (i) A demonstration of the robust adhesion of Gel-GM hydrogel to porcine skin under the following conditions: twisting, bending, and water flushing. (ii) Adhesion performance of Gel-GM to various biological tissues on a glass slide. (b) Schematic illustration of the apparatus utilized for the lap shear test on porcine skin. (c) Representative stress-strain curves for the lap shear test (n = 3). (d) A quantitative comparison of the average lap-shear strength of the hydrogels (n = 3). (e) Molecular model of the Gel-GM hydrogel. (f) The structural evolution of Gel-GM and Gel hydrogel at tensile strains of 25, 50, 75, and 100 ns is demonstrated by MD simulation snapshots. Analysis of MD simulation trajectories: (g) number of hydrogen bonds, (h) solvent-accessible surface area (SASA), and (i) intermolecular interaction energy (free energy decomposition) for Gel-GM and Gel after stretching. (j) Schematic illustration of the Gel-GM hydrogel with strong adhesion. (k) Schematic illustration of the hemostasis process. (l) Photographs of a liver hemorrhage model treated with nothing (Blank) and with Gel-GM. (m) Comparison of blood loss for hemostasis with no treatment and using Gel-GM (n = 3). (n) Blood compatibility was evaluated by hemolysis assay (n = 3). Data represent mean ± SD; *P < 0.05, **P < 0.01, ***P < 0.001, ****P < 0.0001 (Student's t-test or one-way ANOVA).

2.3 Biocompatibility, antioxidant capacity, and macrophage polarization of Gel-GM hydrogels

To further confirm the biocompatibility of the Gel-GM hydrogel, cell viability and proliferation were assessed using live/dead staining (Fig. 3(a)). Results showed no statistically significant differences in cell viability or growth between the Gel-GM-treated group and the control group after 24 h, while the Gel-GM group exhibited significantly higher cell viability at 48 h (Figs. 3(b) and 3(c)). These findings indicate good cell compatibility of the material.

To investigate *in vivo* degradation and biosafety, Gel-GM hydrogel was subcutaneously implanted into the dorsal region of

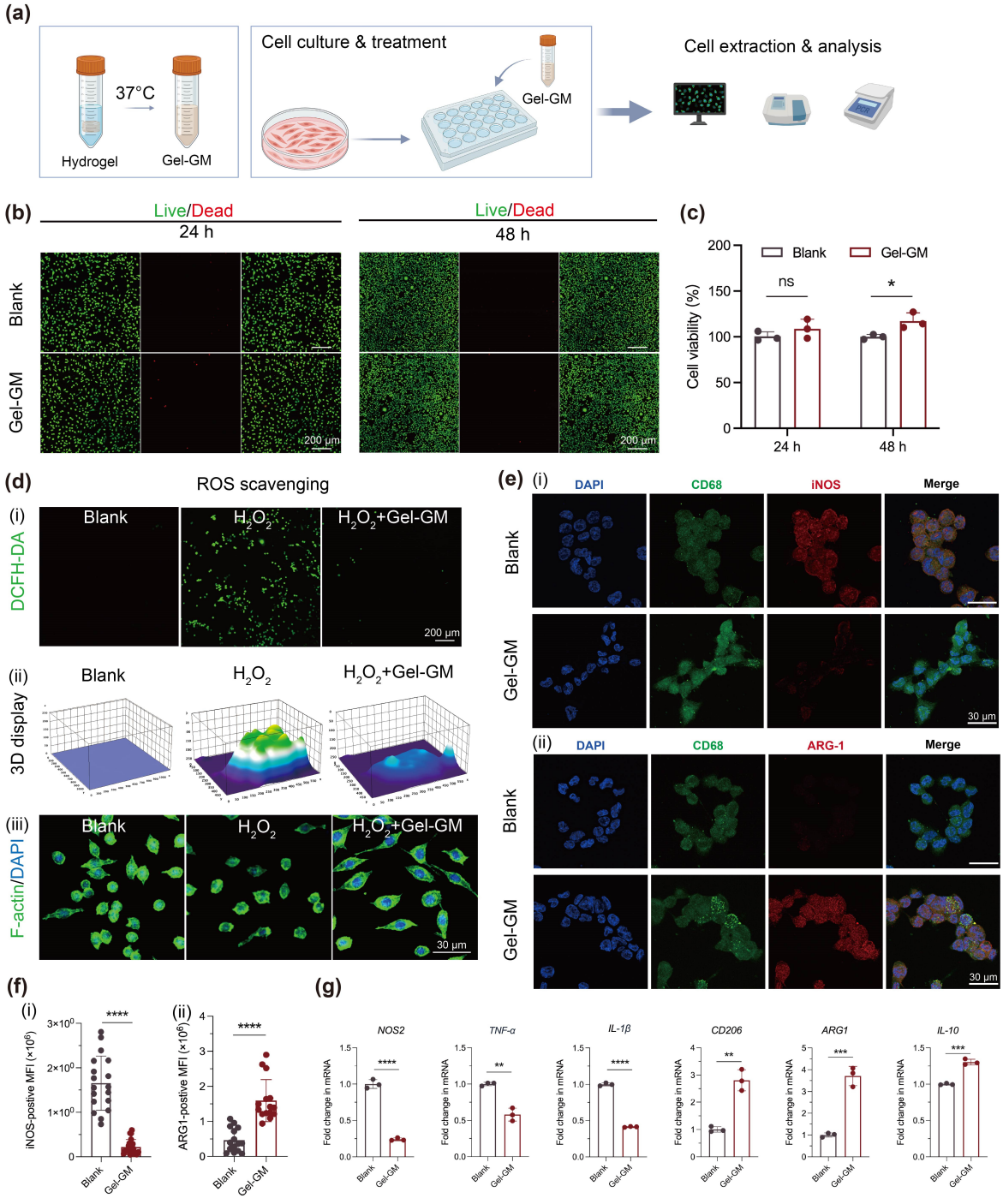


Figure 3 Biocompatibility, antioxidant properties, and macrophage polarization evaluation of Gel-GM hydrogels. (a) Schematic of *in vitro* cell experiments. (b) Live/dead staining images of L929 cells incubated with different treatments (Blank, Gel-GM) for 24 and 48 h. (c) Cell viability of L929 cells after 24 and 48 h incubation with various treatments. (d) Intracellular ROS levels determined by DCFH-DA staining: (i) immunofluorescence (IF) analysis showing relative expression, (ii) spatial distribution, and (iii) cytoskeletal organization visualized by F-actin staining (blue: nuclei; green: cytoskeleton). (e) Representative IF images showing CD68 (green), ARG-1 (red), and iNOS (red) expression in THP-1 cells across different treatments. (f) Quantitative analysis of iNOS/CD68 and ARG-1/CD68 positive cell ratios. (g) Relative mRNA expression levels of *NOS2*, *TNF-α*, *IL-1β*, *CD206*, *ARG-1*, and *IL-10* in macrophages co-cultured with different groups. $n \geq 3$ biologically independent samples. Data represent mean ± SD; $^{*}P < 0.05$, $^{**}P < 0.01$, $^{***}P < 0.001$, $^{****}P < 0.0001$ (Student's *t*-test or two-way ANOVA).

mice, and its degradation process and local tissue responses were monitored at 12, 24, 48, and 72 h post-implantation. Observations showed that the hydrogel remained at the injection site, adhering to the skin surface, with no significant swelling or hemorrhage observed in surrounding tissues (Fig. S6(b) in the ESM). By 72 h, the hydrogel had nearly completely degraded, likely due to accelerated degradation resulting from the lower molecular weight of OSA [31]. Hemostatic adhesives with relatively rapid degradation rates have been demonstrated to promote wound healing and prevent secondary injury associated with dressing changes [32]. Additionally, H&E staining revealed mild inflammatory cell infiltration at the implantation site (Fig. S6(c) in the ESM). These findings indicate that the inflammatory response induced by Gel-GM hydrogel is within an acceptable range, demonstrating good biocompatibility and supporting its feasibility for subsequent *in vivo* applications.

The effect of Gel-GM hydrogel on intracellular oxidative stress was assessed by detecting intracellular ROS using a 2',7'-dichlorodihydrofluorescein diacetate (DCFH-DA) probe. The experimental groups included a positive control (treated with H_2O_2, exhibiting strong fluorescence), a negative control (untreated, showing no fluorescence), and a Gel-GM co-culture group (also treated with H_2O_2). Results revealed significantly reduced intracellular fluorescence intensity in the Gel-GM-treated group compared to the positive control, indicating effective reduction of intracellular ROS levels by Gel-GM hydrogel, thereby improving the oxidative stress microenvironment (Fig. 3(d)).

During chronic infected wound healing, typical pathological changes include increased macrophage infiltration and chronic inflammation. Polarization of macrophages towards the M2 phenotype is critical for mitigating inflammation and promoting angiogenesis [33]. To evaluate whether the Gel-GM hydrogel can induce macrophage polarization from M1 to M2, a lipopolysaccharide (LPS)-induced macrophage inflammation model was used to detect changes in CD68 (M0 marker), inducible nitric oxide synthase (iNOS) (M1 marker), and arginase-1 (ARG-1) (M2 marker) expression. Results showed high iNOS expression and a high proportion of M1 macrophages in the Blank control group, whereas the Gel-GM-treated group exhibited significantly increased ARG-1 expression and a markedly higher proportion of M2 macrophages (Fig. 3(e)), demonstrating the hydrogel's ability to promote M2 macrophage polarization. Quantitative analysis revealed a significant decrease in iNOS-positive cells accompanied by a corresponding increase in ARG-1-positive cells following Gel-GM hydrogel treatment (Fig. 3(f)). Furthermore, quantitative polymerase chain reaction (qPCR) results supported these findings, with the Gel-GM group showing significantly reduced mRNA expression of pro-inflammatory factors (*NOS2*, *IL-1β*, *TNF-α*) and significantly increased expression of anti-inflammatory factors (*CD206*, *ARG-1*, *IL-10*) compared to the Blank group (Fig. 3(g)). These findings indicate that Gel-GM hydrogel effectively remodels the inflammatory microenvironment by modulating inflammation-related factor expression, promoting M2 macrophage polarization, and exerting anti-inflammatory effects.

2.4 Mechanistic insight into fibroblast phenotypic switching via RNA-seq analysis

Cell migration is a critical process in wound healing regulation. In this study, a cell scratch assay was employed to simulate *in vitro* wound healing and evaluate the effect of Gel-GM hydrogel on L929 cell migration (Fig. 4(a)). Results indicated that, from 6 h onwards, Gel-GM hydrogel significantly accelerated the migration rate of L929 cells (Fig. 4(b)), with marked effects at 12 and 24 h. By 24 h, the average migration enhancement reached 70.15% (Fig. 4(c)). Previous studies have indicated that catechol presence promotes cell migration [34], possibly due to strong interactions with imidazole or thiol groups on fibroblast membranes [35–37]. These interactions may regulate intracellular signaling pathways, thereby enhancing cell migration. To further elucidate the molecular mechanisms underlying the Gel-GM hydrogel's promotion of cell migration, total RNA was extracted from L929 cells co-cultured with the hydrogel for 24 h and subjected to transcriptome sequencing (Fig. 4(d)). Principal component analysis (PCA) showed good reproducibility among samples within groups (Fig. 4(e)). Differential gene expression analysis identified 1171 differentially expressed genes (DEGs), comprising 790 significantly upregulated and 381 significantly downregulated genes. For functional insights, Gene Ontology (GO) and Kyoto Encyclopedia of Genes and Genomes (KEGG) pathway enrichment analyses were performed on the DEGs (Figs. 4(f) and 4(g)). GO enrichment analysis highlighted significant enrichment in the cell migration pathway, suggesting modulation of migration-related gene expression by the Gel-GM hydrogel. Several cell migration-related genes were significantly upregulated in the Gel-GM group, including *Ccl20*, *Lcp1*, *Trem3*, *Tnfaip3*, *Cass4*, *Adgrg1*, *Gfra1*, and *Coro6* (Fig. 4(h)). Notably, chemokine *Ccl20* showed the most significant expression change, detected exclusively in the Gel-GM group with notable fold change (FC) upregulation. Previous studies have confirmed that CCL20 primarily mediates cell migration and inflammation regulation by forming a signaling axis with its receptor C-C chemokine receptor type 6 (CCR6).

In fibroblasts, the CCL20-CCR6 axis synergistically regulates key repair processes, such as cell migration, proliferation, and ECM remodeling, thus playing a crucial role in wound healing [38]. Additionally, in a corneal epithelial injury model, rapid upregulation of CCL20 recruits CCR6-positive *γδ*T cells, directly promoting epithelial cell proliferation and wound closure, further supporting its central role in tissue repair [39]. We speculate that *Ccl20* upregulation observed in the Gel-GM group exerts a similar effect. Notably, aside from cell migration, GO enrichment analysis indicated that DEGs were significantly enriched in multiple ECM-related terms, including ECM (false discovery rate (FDR) < 0.001), collagen-containing ECM (FDR < 0.001), and ECM structural constituent (FDR < 0.001). These results suggest that Gel-GM hydrogel may regulate cell behavior by influencing ECM remodeling. Moreover, GSEA analysis demonstrated significant suppression of these GO terms in the Gel-GM hydrogel-treated group: ECM (normalized enrichment score (NES) = −1.913, P < 0.001), collagen-containing ECM (NES = −1.973, P < 0.001), and ECM structural constituent (NES = −1.877, P < 0.001) (Fig. 4(j)). We hypothesize that this state resembles the early stage of tissue injury repair, during which cells degrade old or damaged ECM components to create migration channels and initiate repair processes. We found that Gel-GM hydrogel treatment upregulated the expression level of matrix metalloproteinase *Mmp13* (a key enzyme for ECM degradation) by nearly 40-fold ($\log_2$(Fold change) = 5.3, FDR = 0.001). The significant transcriptional upregulation of *Mmp13* is associated with enhanced fibroblast migration and subsequent tissue remodeling, consistent with the established pro-migratory role of MMP13 in wound repair [40]; however, a causal relationship remains to be established through functional loss-of-function experiments.

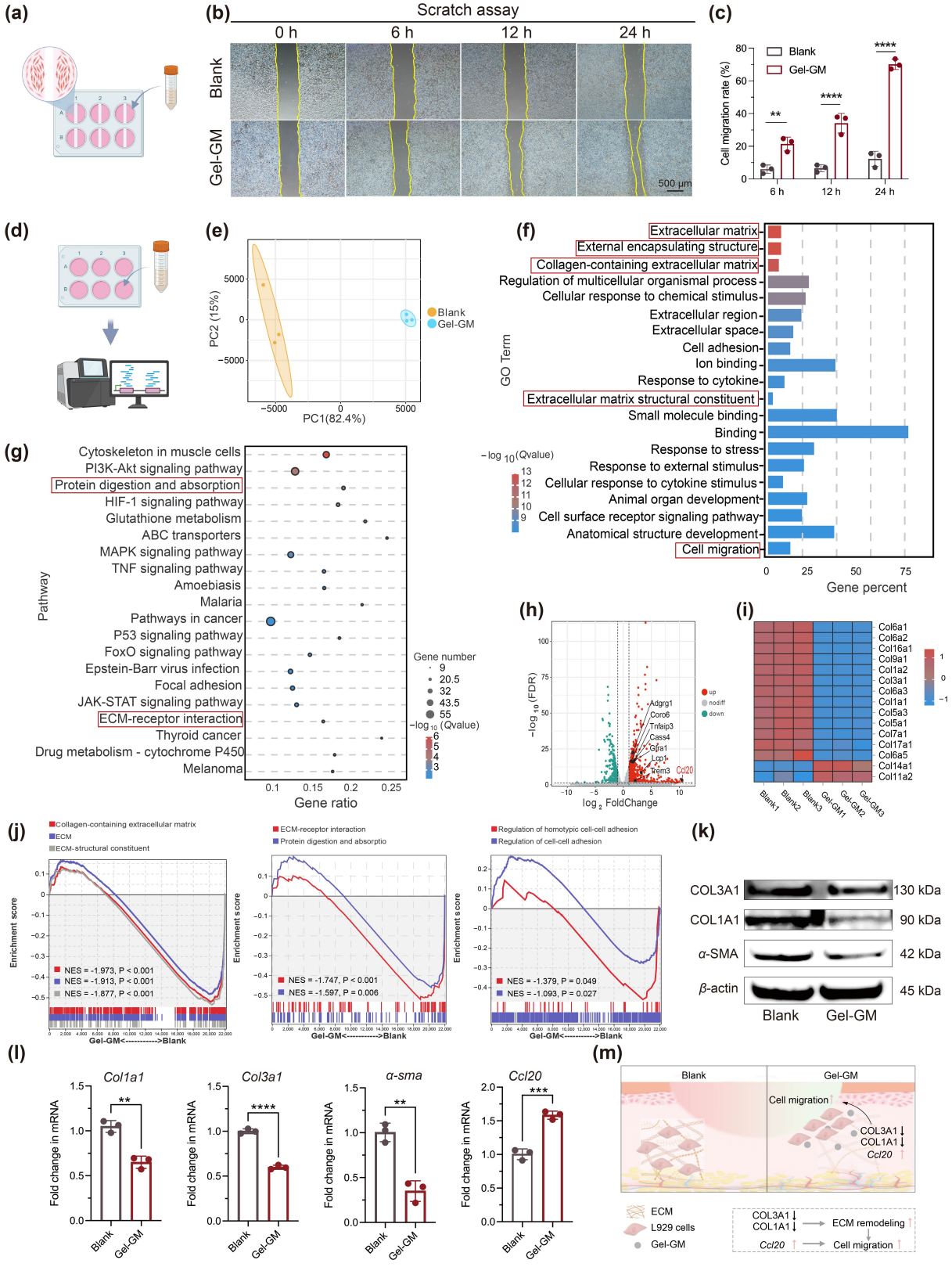


Figure 4 Cell migration, RNA-seq, and mechanism analysis. (a) Schematic diagram of cell migration *in vitro*. (b) Images of wound scratch migration assay. (c) Quantification of L929 cell migration (Blank, Gel-GM groups). (d) Schematic of RNA-seq experimental design. RNA from L929 cells (Blank and Gel-GM treated) was sequenced using the Illumina platform. (e) PCA of RNA-seq data (Blank, Gel-GM groups). (f) KEGG pathway enrichment analysis of DEGs. (g) GO enrichment analysis of DEGs. (h) Volcano plot of RNA-seq data (red points: upregulated genes, blue points: downregulated genes; criteria: $\log_2$(Fold change) > 1 or < −1, FDR < 0.05). (i) Heatmap of representative collagen-encoding genes. (j) Gene Set Enrichment Analysis (GSEA) showing enrichment of ECM and cell adhesion gene sets in Gel-GM-treated cells. Verification of DEGs by (k) Western blot and (l) qPCR, respectively. (m) Schematic diagram illustrating the mechanism of enhanced cell migration following Gel-GM treatment. Data represent mean ± SD ($n = 3$); *$P < 0.05$, **$P < 0.01$, ***$P < 0.001$, ****$P < 0.0001$ (Student's *t*-test or two-way ANOVA).

Additionally, KEGG pathway enrichment analysis indicated that DEGs were significantly enriched in ECM-receptor interaction (FDR < 0.001) and protein digestion and absorption (FDR = 0.005) pathways. Correspondingly, GSEA analysis showed downregulation of these pathways (ECM-receptor interaction: NES = −1.747, P < 0.001; protein digestion and absorption: NES = −1.597, P = 0.006), suggesting inhibited ECM synthesis, consistent with GO enrichment results (Fig. 4(j)). Furthermore, gene expression heatmaps revealed significant downregulation of multiple collagen-encoding genes (e.g., *Col1a1*, *Col3a1*) (Fig. 4(i)). Collectively, these data suggest that the catechol-sodium alginate component of Gel-GM hydrogel directs fibroblast behavior towards an early repair state characterized primarily by migration, through regulation of ECM degradation. GO enrichment analysis also revealed significant enrichment of DEGs in cell adhesion-related terms (FDR < 0.001), with notable suppression of regulation of cell-cell adhesion (NES = −1.093, P = 0.027) and regulation of homotypic cell-cell adhesion (NES = −1.379, P = 0.049) (Fig. 4(j)). This weakening of cell adhesion is hypothesized as an adaptive regulatory mechanism allowing fibroblasts to gain motility. Early in wound healing, fibroblasts transiently detach from tight intercellular connections, transitioning from a static adhesion phenotype to a dynamic migratory phenotype, facilitating directional recruitment to injury sites.

To validate the reliability of the transcriptome sequencing results, key genes (*Col1a1*, *Col3a1*, *α-sma*, and *Ccl20*) were analyzed using real-time quantitative polymerase chain reaction (RT-qPCR) and Western blotting. Western blot analysis showed decreased protein levels of COL1A1, COL3A1, and alpha-smooth muscle actin (α-SMA) in the Gel-GM group compared with the Blank group (Fig. 4(k)), aligning with the transcriptomic findings of suppressed ECM synthesis and reduced cell-cell adhesion. RT-qPCR similarly demonstrated lower mRNA expression of *Col1a1*, *Col3a1*, and *α-sma*, accompanied by significant upregulation of *Ccl20* in the Gel-GM group (Fig. 4(l)). Collectively, these results indicate that Gel-GM hydrogel concurrently inhibits ECM synthesis-related and myofibroblast-associated markers, while activating the migration-promoting chemokine CCL20, thus promoting a migratory fibroblast phenotype in the early phase of wound repair. In summary, the data suggest that Gel-GM hydrogel facilitates fibroblast migration through mechanisms driven by the catechol-sodium alginate component. This involves transcriptional induction of *Mmp13*, potentially aiding ECM remodeling, suppression of cell-cell adhesion to enable cell motility, and activation of migration-associated gene expression, collectively enhancing fibroblast recruitment to injury sites (Fig. 4(m)). Within this regulatory network, *Ccl20* displays the most pronounced transcriptional change, highlighting its possible central role in mediating fibroblast migration, a hypothesis that warrants subsequent protein-level validation. A notable limitation of this study is that, although *Ccl20* was identified as the most significantly upregulated migration-associated gene in Gel-GM-treated fibroblasts, and despite its well-established role in wound repair through the CCL20-CCR6 axis in fibroblast, epithelial, and immune cell contexts, we did not perform loss-of-function experiments to causally link its upregulation to Gel-GM-enhanced fibroblast motility. While our transcriptomic and biochemical validations support a correlative association, the necessity of the CCL20-CCR6 axis in this context remains to be definitively established. Future investigations employing fibroblast-specific *Ccl20* knockdown or pharmacological inhibition of CCR6 are warranted to clarify its precise contribution to Gel-GM-mediated tissue repair.

2.5 Antibacterial capability of Gel-GM hydrogels *in vitro*

Chronic infected wounds are frequently complicated by bacterial infections, posing significant challenges for wound healing. Therefore, excellent antibacterial properties are crucial for wound adhesive hydrogels [41]. The antibacterial capability of Gel-GM hydrogel against *Staphylococcus aureus* (*S. aureus*) and *Escherichia coli* (*E. coli*) was evaluated *in vitro* (Fig. 5(a)). Bacterial colony counting indicated nearly 100% bacterial viability in the Blank group, whereas colony counts significantly decreased in the Gel-GM group, showing bacterial viability rates of 0.33% and 3.93% for *S. aureus* and *E. coli*, respectively (Fig. 5(b)), thereby demonstrating superior antibacterial performance.

Furthermore, bacterial viability was assessed using the SYTO 9 green fluorescent nucleic acid stain and the propidium iodide (PI) red fluorescent nucleic acid stain. SYTO 9 stains all bacteria, whereas PI selectively penetrates compromised cell membranes, staining only dead bacteria. Consequently, live bacteria fluoresce green, while dead bacteria fluoresce red. The Blank group exhibited exclusively green fluorescence, while the Gel-GM group showed minimal green fluorescence and substantial red fluorescence, indicating bacterial death and membrane disruption (Fig. 5(c)).

SEM and TEM analyses further elucidated the bactericidal mechanism of Gel-GM hydrogel. SEM observations (Fig. 5(d)) revealed that *S. aureus* (spherical) and *E. coli* (rod-shaped) exhibited intact cell membranes in the Blank group. In contrast, bacteria treated with Gel-GM displayed shrunken morphology and structural disruption (white arrows). TEM imaging (Fig. 5(e)) showed intact, clearly defined cell membranes and dense internal structures in the Blank group bacteria, whereas the Gel-GM-treated group exhibited ruptured and separated cell membranes, accompanied by leakage of cellular contents (yellow arrows). Collectively, these findings demonstrate the exceptional antibacterial activity of Gel-GM hydrogel, attributable to the incorporation of the AMP LL-37. LL-37 carries a positive charge ($-NH_3^+$) and effectively interacts with negatively charged bacterial cell membranes, forming membrane pores and compromising membrane integrity. This action results in membrane damage, intracellular leakage, and ultimately, bacterial death [42, 43].

2.6 Gel-GM hydrogels promoted infected wound healing by modulating M2 macrophage polarization

In vitro experiments have confirmed the antioxidant activity, tissue adhesion capability, biocompatibility, M2 macrophage polarization ability, and antibacterial performance of Gel-GM hydrogel, demonstrating its broad potential for infected wound management. Therefore, the therapeutic efficacy of Gel-GM hydrogel in skin healing was further evaluated using an infected full-thickness skin defect model (Fig. 6(a)).

Initially, a 6-mm full-thickness defect was created on the mouse dorsum, and an infected wound model was established by injecting 50 μL of an *S. aureus* suspension (1×10^8 CFU/mL). Representative images were collected at days 0, 3, 7, and 14 to monitor and quantify therapeutic effects (Figs. 6(b) and 6(c)). After 7 days, the Gel-GM group exhibited the smallest remaining wound area (19.80% unhealed), demonstrating significantly enhanced therapeutic efficacy. In contrast, the control group and Gel group showed larger residual unhealed areas of 58.45% and 31.90%,

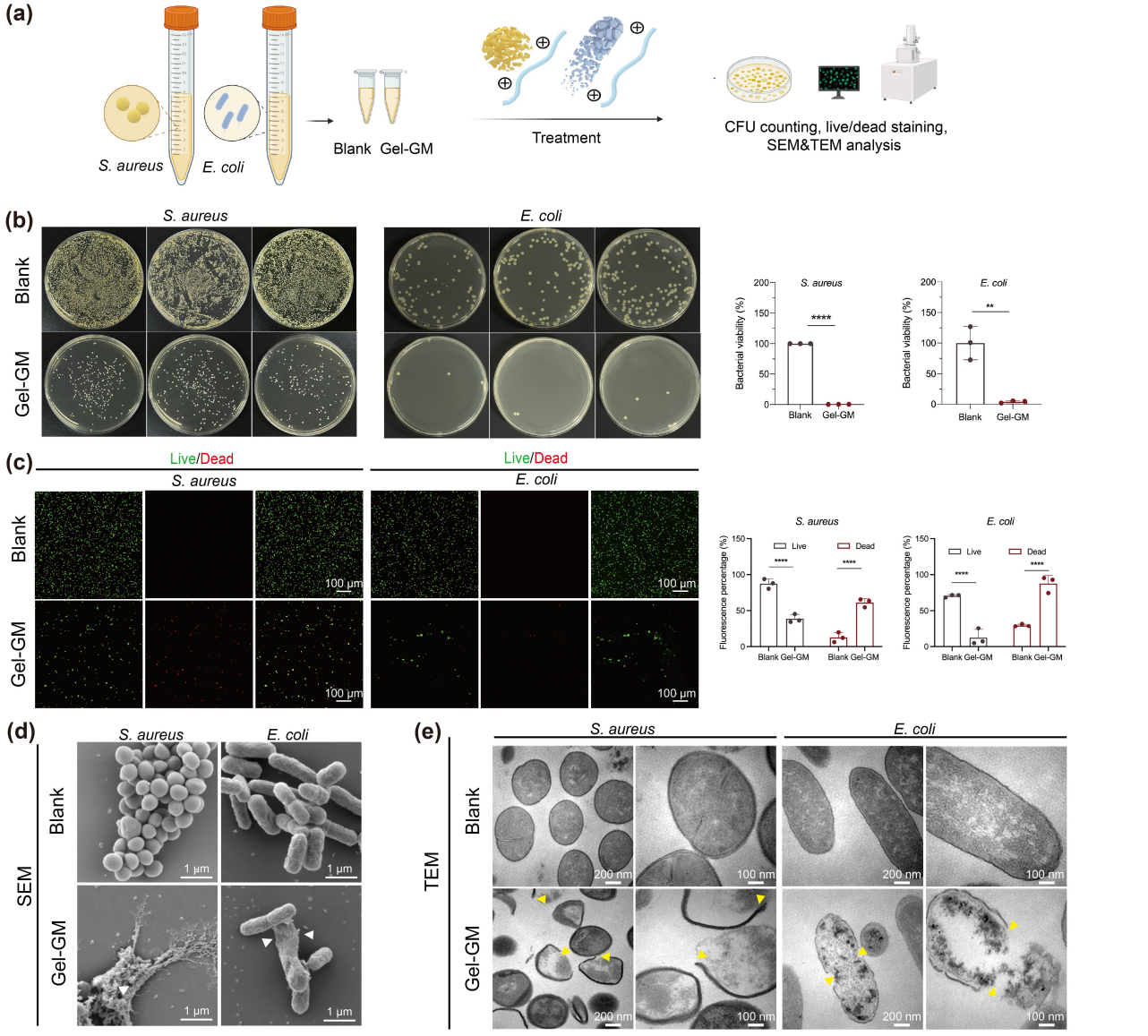


Figure 5 Antibacterial activity of Gel-GM hydrogels *in vitro*. (a) Schematic of experimental procedure and proposed antibacterial mechanism. (b) Representative images of colony-forming units (CFU) and quantitative analysis of bacterial viability of *S. aureus* and *E. coli* under various treatments. (c) Bacterial viability assessed by live/dead staining and quantitative analysis. Morphological analyses using (d) SEM and (e) transmission electron microscopy (TEM). White and yellow arrows indicate damaged bacterial cell membranes. Data represent mean ± SD ($n = 3$); *$P < 0.05$, **$P < 0.01$, ***$P < 0.001$, ****$P < 0.0001$ (Student's *t*-test).

respectively, indicating delayed healing. By day 14, the Gel-GM group exhibited a residual wound area of only 1.33% (Fig. 6(e)). This accelerated healing was attributed to effective wound sealing due to strong tissue adhesion from catechol groups in the Gel-GM hydrogel and sustained antibacterial activity from encapsulated LL-37, both critical factors in the early wound-healing stages. Furthermore, bacterial inoculation of wound margins on agar plates at day 10 confirmed complete bacterial clearance in the Gel-GM group, validating the hydrogel's *in vivo* antimicrobial efficacy (Fig. 6(d)). These findings confirm that Gel-GM hydrogel simultaneously possesses antibacterial and pro-healing properties in infected wound healing.

To further explore the mechanisms underlying Gel-GM's promotion of infected wound healing, histological and immunological analyses of regenerated skin were conducted at different time points. Hematoxylin and eosin (H&E) staining demonstrated that wound contraction was most pronounced on day 7 (Fig. 6(f)). H&E and Masson's trichrome staining on day 14 (Fig. 6(g)) revealed that the Blank control group displayed only superficial epidermal regeneration accompanied by substantial inflammation. Conversely, the Gel-GM group exhibited optimal healing outcomes, characterized by dense epidermal tissue, well-organized dermal structure, and clearly visible mature skin appendages such as hair follicles. Masson's staining further indicated increased collagen deposition and better-organized fibrous structure in the Gel-GM group.

To further elucidate the progression of wound healing, IF and immunohistochemistry (IHC) analyses were performed. Ki67 IF staining, used to assess epidermal basal cell proliferation, a key factor in wound re-epithelialization, revealed significantly increased expression in the Gel-GM group (Fig. S4(a) in the ESM). Additionally, macrophage polarization from a pro-inflammatory

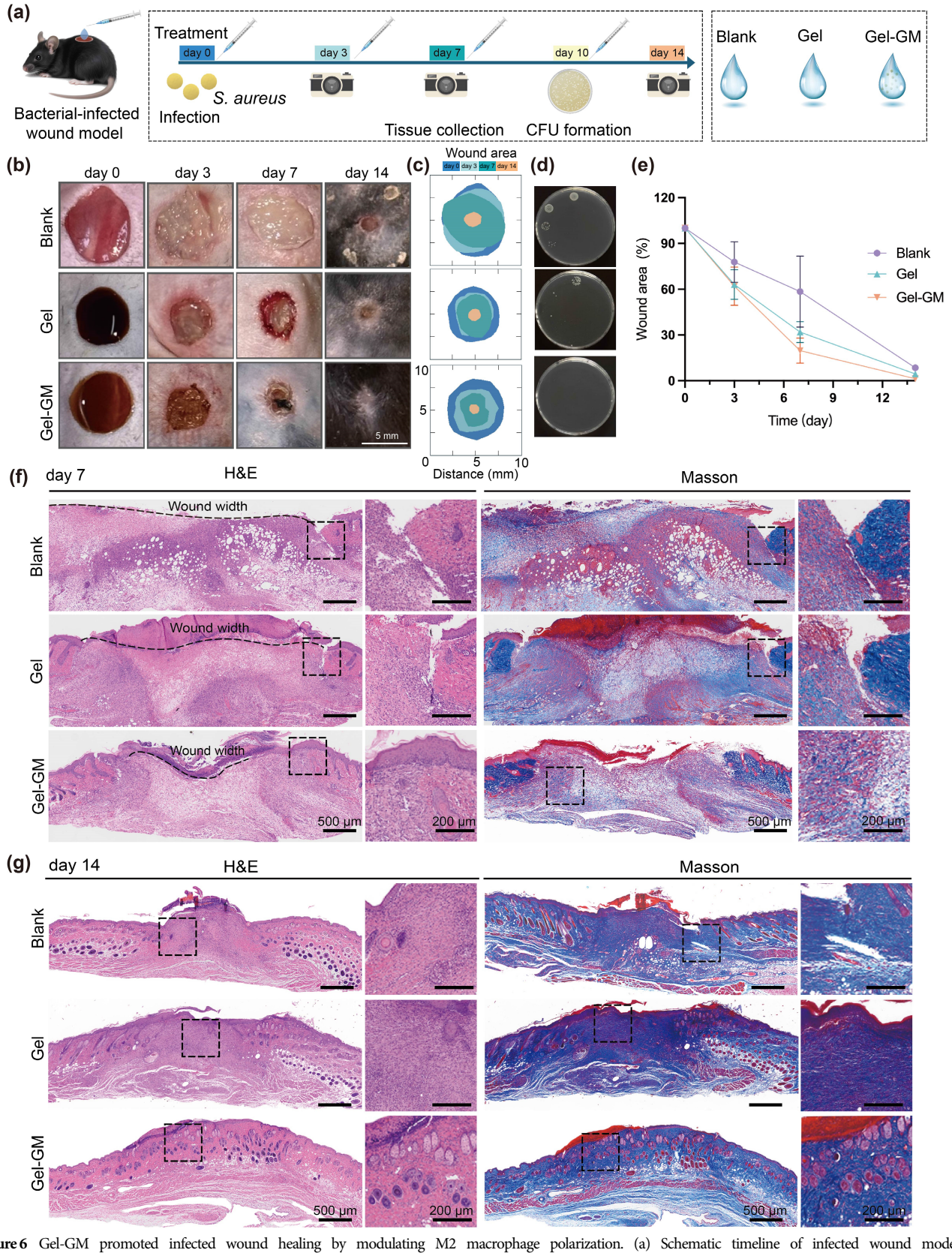


Figure 6 Gel-GM promoted infected wound healing by modulating M2 macrophage polarization. (a) Schematic timeline of infected wound modeling. (b) Representative wound images from PBS (Blank), Gel, and Gel-GM groups at days 0, 3, 7, and 14. (c) Simulated images of corresponding wound areas under different treatments at days 0, 3, 7, and 14. (d) Photographs of *S. aureus* colonies cultured from wound margins on day 10. (e) Residual wound area at indicated time points for each group. (f) Representative H&E and Masson's trichrome staining of wound tissues on day 7 (black dotted lines indicate wound width). (g) Representative H&E and Masson's trichrome staining images from different treatments on day 14 ($n = 3$).

M1 phenotype to a pro-healing M2 phenotype is critical for resolving inflammation and regenerating skin tissue. IF imaging showed extensive distribution of M2 macrophages (CD206-positive), and a significantly reduced number of M1 macrophages were observed in the Gel-GM group (Fig. 7(a)). Evaluation of inflammatory cytokines revealed significantly increased expression of anti-inflammatory IL-10 and decreased levels of pro-inflammatory tumor necrosis factor-alpha (TNF-α) in the Gel-GM group relative to the Blank group (Fig. 7(b)), consistent with *in vitro* observations. Compared with the Blank group, Gel-GM-treated wounds exhibited reduced subcutaneous inflammation (Figs. 7(e)–7(g)), indicating that Gel-GM hydrogel attenuates inflammatory responses during early healing stages, creating a favorable healing environment. Vascularization, an essential indicator of tissue regeneration and infected wound healing, was assessed using CD31 and α-SMA markers. By day 7, the Gel-GM hydrogel significantly increased the expression of both α-SMA (Fig. S4(b) in the ESM) and CD31 (Fig. 7(c)) in regenerated skin tissue, demonstrating enhanced angiogenesis (Fig. 7(h)). Notably, the early fibroblast-specific decline in α-SMA promotes matrix remodeling, whereas the later pericytic increase signifies vascular maturation, thereby reconciling the temporal and cell type discrepancy. Analysis of collagen composition provided further insights into wound healing progression. Sirius Red staining revealed significantly higher proportions of mature type I collagen fibers in the Gel-GM group compared with the Blank group (Fig. 7(d)). Finally, H&E staining showed no evident morphological abnormalities in the major organs of the Gel-GM group compared with the Blank group (Fig. S6(d) in the ESM), confirming the biosafety of Gel-GM hydrogel *in vivo*.

The therapeutic efficacy of Gel-GM arises from a tripartite synergy among porous GMs, catechol groups, and LL-37, each playing orthogonal yet mutually reinforcing roles. Structurally, GMs strengthen the hydrogel network by enhancing intermolecular interactions, as confirmed by MD simulations, thus optimizing cohesive strength while ensuring catechol groups remain surface-exposed rather than trapped within an overly crosslinked matrix. Consistent with this structural design, Gel-GM maintains the

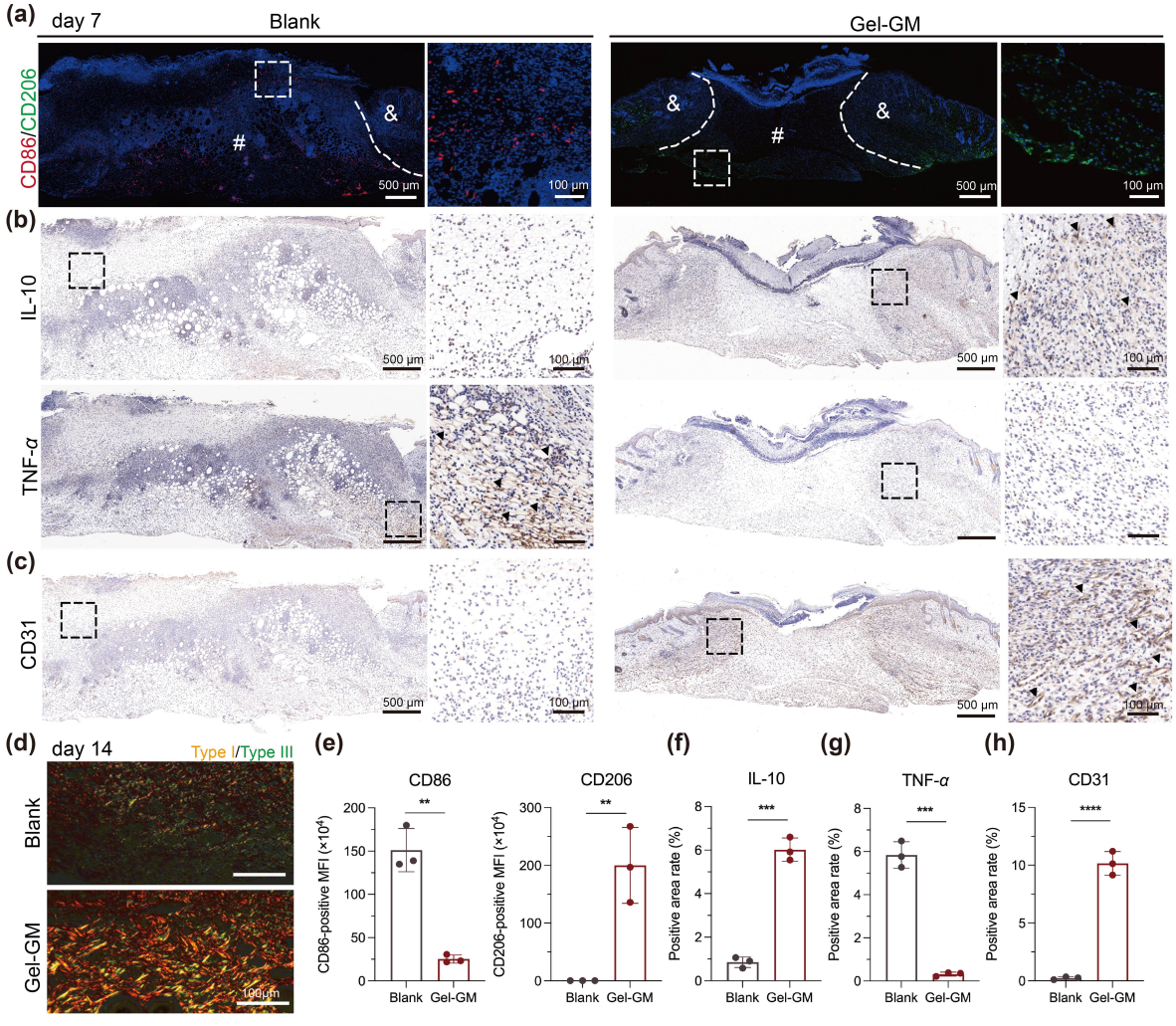


Figure 7 Mechanisms underlying infected wound healing at day 7 following Gel-GM hydrogel treatment. (a) Representative IF images demonstrating macrophage polarization, with M1 (CD86, red) and M2 (CD206, green) markers. (b) IHC staining for the pro-inflammatory cytokine TNF-α and anti-inflammatory cytokine IL-10 in regenerated skin tissue from each group. (c) CD31 IHC staining labeling vascular endothelial cells to indicate angiogenesis. (d) Sirius Red staining for collagen (collagen I marked by orange-red; collagen III marked by green). Quantitative analysis results of IF and IHC staining images of (e) CD86 and CD206, (f) IL-10, (g) TNF-α, and (h) CD31. #: regenerated granulation tissue; &: normal skin edges; dotted lines: boundary between normal skin and wound area; blank arrows: positive staining. Data represent mean ± SD ($n = 3$); $^*P < 0.05$, $^{**}P < 0.01$, $^{***}P < 0.001$, $^{****}P < 0.0001$ (Student's t-test).

bioactivity of catechol groups: it retains antioxidant capacity comparable to the GM-free Gel and continues to induce M2 macrophage polarization *in vitro* and an anti-inflammatory cytokine profile *in vivo*. Functionally, the porous architecture of GMs likely serves as a reservoir for the cationic AMP LL-37, sustaining its bioavailability at the wound interface [44, 45]. Although direct LL-37 release kinetics were not quantified in this study, due to matrix interference with peptide-quantification assays and electrostatic complexity between cationic LL-37 and the anionic OSADA network [46, 47], the absence of *S. aureus* colonies at the Gel-GM wound margin by day 10 (Fig. 6(d)) provides indirect functional evidence of prolonged LL-37 availability. Future studies will directly quantify LL-37 release kinetics from Gel-GM hydrogels.

Overall, the Gel-GM hydrogel promotes chronic infected wound healing by reshaping the immune microenvironment, simultaneously alleviating oxidative stress, suppressing inflammation, and eliminating bacteria. This hydrogel demonstrates significant promise as an innovative dressing for chronic infected wounds. Future efforts will focus on optimizing the adhesive strength of catechol-based hydrogel dressings, balancing cohesive and adhesive properties, and elucidating underlying biological mechanisms involved in tissue regeneration.

3 Conclusions

Infected wounds represent a significant clinical challenge due to their complex microenvironment characterized by persistent infection, excessive ROS, and dysregulated inflammation. To address these multifaceted demands, we successfully developed a porous GM-reinforced adhesive hydrogel (Gel-GM) based on a cohesion-adhesion balance strategy, providing comprehensive wound management. Gel-GM hydrogels achieve therapeutic efficacy via the following mechanisms: embedded microspheres form a denser, dynamic network structure that enhances cohesive strength and interfacial adhesion, ensuring sustained wound sealing and adaptability to irregular tissue surfaces; exposed catechol groups effectively scavenge ROS and guide macrophage polarization towards the regenerative M2 phenotype, thereby reshaping the inflammatory microenvironment; integrating GMs as a cellular scaffold with LL-37 provides a pro-regenerative immune environment and potent infection control; transcriptomic analysis further revealed that Gel-GM promotes fibroblast migration, identifying upregulated *Ccl20* expression as a potential key regulator.

This study validates the cohesion-adhesion balance strategy as an effective approach for designing novel adhesive hydrogel materials, resolving the mechanical strength-interfacial adhesion trade-off inherent in catechol-based hydrogels. By actively participating in the entire wound healing process, from initial infection control and inflammation regulation to subsequent tissue remodeling, the hydrogel overcomes limitations associated with traditional passive dressings. However, precise molecular mechanisms through which Gel-GM regulates *Ccl20* expression and subsequent cell migration require further elucidation. Moreover, evaluating long-term safety, degradation kinetics, and translational potential will necessitate studies employing large animal models and clinical trials. Gel-GM hydrogels represent a substantial advancement towards intelligent, multifunctional hydrogel dressings. Future perspectives in this field include the development of medical wound patches exhibiting dynamic adaptability to evolving pathophysiological states in infected wounds.

4 Experimental

4.1 Fabrication and characterization of Gel-GM hydrogel

Gel-GM hydrogel was prepared by incorporating GMs and the AMP LL-37 into the OSADA solution, followed by crosslinking with $NaIO_4$ solution. The composition and mixing ratios of each group are listed in Table S1 in the ESM. The surface morphology of the hydrogel was characterized using SEM (JEOL, Japan).

4.2 Rheological measurements

The rheological properties of the hydrogels, including the storage modulus (G') and loss modulus (G''), were evaluated using a rheometer (MCR302, Anton Paar, Germany) equipped with a 25-mm parallel plate. To determine the viscoelastic region of the hydrogels, strain sweep measurements were performed under oscillatory strain ranging from 1% to 1500% at a fixed frequency of 1 Hz. Time sweep experiments were conducted at a constant frequency (1 Hz) and strain (1%). The self-healing properties of the hydrogels were evaluated using alternating step-strain sweep tests under 1% and 400% strain at 1 Hz.

4.3 DPPH radical scavenging activity

The materials were mixed with DPPH ethanol solution and allowed to react for 30 min. Absorbance spectra within the 200–1000 nm range were subsequently measured using a microplate reader (VICTOR Nivo). DPPH scavenging efficiency was calculated based on the optical density (OD) at 517 nm using the following equation (Eq. (1)):

$$\text{DPPH scavenging rate}\ (\%) = \frac{A_{\text{DPPH}} - A_{\text{Test}}}{A_{\text{DPPH}}} \times 100\% \quad (1)$$

where A_{DPPH} represents the OD value of untreated DPPH solution and A_{Test} represents the OD value after material treatment.

4.4 $ABTS^+$ radical scavenging activity

The $ABTS^+$ stock solution was prepared and incubated in the dark at room temperature for 12–16 h before use. Absorbance spectra within the 200–1000 nm range were measured using a microplate reader (VICTOR Nivo). $ABTS^+$ scavenging efficiency was calculated according to the OD at 734 nm using the following equation (Eq. (2)):

$$ABTS^{\cdot+}\ \text{scavenging rate}\ (\%) = \frac{A_{ABTS^{\cdot+}} - A_{\text{Test}}}{A_{ABTS^{\cdot+}}} \times 100\% \quad (2)$$

where $A_{ABTS^{\cdot+}}$ represents the OD value of untreated $ABTS^+$ solution, and A_{Test} represents the OD value after material treatment.

4.5 Hemocompatibility evaluation

Hemocompatibility was evaluated using a hemolysis assay with red blood cells (RBCs). Fresh blood was collected from the hearts of Sprague-Dawley rats into EDTA-anticoagulated tubes. The blood samples were washed three times with physiological saline (0.9% NaCl) at 2000 rpm for 10 min and subsequently diluted to obtain a 5% (v/v) RBC suspension. For the negative control group, 200 μL RBC suspension was mixed with 800 μL physiological saline. For the positive control group, 200 μL RBC suspension was mixed with

800 μL 0.1% Triton X-100. The experimental group consisted of 200 μL RBC suspension, 100 μL hydrogel, and 700 μL physiological saline. All mixtures were incubated at 37 °C for 1 h, followed by centrifugation at 2000 rpm for 10 min. Hemolysis was visually observed and photographed. Subsequently, 100 μL of the supernatant from each sample was transferred into a 96-well plate, and absorbance at 540 nm was measured using a microplate reader (VICTOR Nivo). Each group contained three parallel samples. The hemolysis rate (HR) was calculated using Eq. (3):

$$\text{Hemolysis}\ (\%) = \frac{\text{OD}_{\text{test}} - \text{OD}_{\text{negative}}}{\text{OD}_{\text{positive}} - \text{OD}_{\text{negative}}} \times 100\% \quad (3)$$

where OD_{test}, $\text{OD}_{\text{negative}}$, and $\text{OD}_{\text{positive}}$ represent the absorbance values at 540 nm for the experimental, negative control, and positive control groups, respectively.

4.6 Adhesion test

Porcine skin and murine organs (heart, liver, spleen, lungs, and kidneys) were used to qualitatively evaluate the adhesive properties of the hydrogels. Detailed methods are provided in the ESM. For quantitative assessment, lap shear tests were performed according to previously reported protocols. Fresh porcine skin was thawed in phosphate-buffered saline (PBS) solution at room temperature for approximately 1 h, cut into 3 × 1 cm slices, and excess fat was carefully removed. The prepared slices were re-immersed in PBS to maintain moisture. Before testing, slices were blotted dry with filter paper, and 200 μL of hydrogel was uniformly spread on one slice over a 1 cm × 1 cm area using a spatula. The second slice was immediately pressed onto the hydrogel-coated area under a 200 g load and incubated for 1 h at 37 °C in a humid environment. Lap shear strength was measured at the point of failure using a universal mechanical testing machine (EZ-LX HS) at a strain rate of 0.5 mm/min. Each group underwent multiple measurements to ensure reliability.

4.7 MD simulations

MD simulations were conducted using Amber 24 software. The hydrogel model was constructed using PACKMOL and solvated with the TIP3P water model, employing the general AMBER force field 2 (GAFF2) force field. Following energy minimization, the system underwent sequential equilibration under NVT (300 K, 30 ps) and NPT (300 K, 1 bar, 30 ps) ensembles, prior to a 100-ns production simulation. Key parameters included a 2 fs integration time step, electrostatic interactions handled by the particle mesh ewald (PME) method (cutoff 1.2 nm), and hydrogen bonds constrained using the LINCS algorithm. Structural evolution was assessed by monitoring the SASA and visualized using PyMOL. Further details are provided in the ESM.

4.8 Hemostasis *in vivo*

A liver hemorrhage model in Sprague-Dawley rats (250–300 g) was employed to assess the hemostatic efficacy of the hydrogels. Rats were anesthetized and stabilized before making an abdominal incision to expose the liver. After carefully removing excess fluid, pre-weighed filter paper was positioned beneath the liver. Bleeding was induced using a 21-gauge needle, immediately followed by application of 50 μL hydrogel onto the wound. The Blank group received needle puncture without subsequent treatment. After 10 min, the filter paper was weighed to quantify absorbed blood. Each experiment was conducted in triplicate.

4.9 Cell compatibility study *in vitro*

Fibroblasts, which play a critical role in skin repair, were used to evaluate hydrogel compatibility. Cell viability was assessed using L929 cells by performing live/dead staining assays and the cell counting kit-8 (CCK-8) method.

4.10 Intracellular ROS scavenging assay

The intracellular ROS scavenging capability of hydrogel samples was evaluated using the DCFH-DA probe. Cells cultured in 6-well plates were treated with hydrogen peroxide and hydrogel extracts. After 12 h incubation, DCFH-DA solution was added for an additional 20 min, followed by fluorescence imaging across different treatment groups.

4.11 *In vitro* anti-inflammatory study

Human monocytic leukemia cell line (THP-1) cells were seeded and stimulated with 100 ng/mL LPS. After LPS stimulation, cells were co-cultured with hydrogel extracts for 24 h. Samples were subsequently fixed in 4% paraformaldehyde for 20 min, permeabilized with 0.1% Triton X-100 solution for 10–15 min, and blocked with 5% bovine serum albumin (BSA) for 30–60 min at room temperature. Diluted primary antibodies targeting iNOS, ARG-1, and CD68 were applied and incubated overnight at 4 °C. Fluorescently labeled secondary antibodies diluted in blocking solution were then added and incubated in the dark for 1 h. After thorough PBS washing in light-protected conditions, antifade mounting medium containing DAPI was applied to stain cell nuclei. Samples were visualized using fluorescence microscopy.

4.12 qRT-PCR

Cells were seeded into 24-well plates. Following adherence, cells were treated with hydrogel extracts for 24 h. Total RNA extraction was performed using the RNAeasy™ Animal RNA Isolation Kit (spin column method). RNA purity and concentration were quantified using a NanoDrop 8000 spectrophotometer. Reverse transcription of RNA into cDNA utilized the PrimeScript RT Reagent Kit, and qPCR assays were conducted using SYBR Green qPCR premix. Primer sequences for target genes are listed in Table S2 in the ESM. Target gene expression was quantified using the $2^{-\Delta\Delta Ct}$ method, with glyceraldehyde-3-phosphate dehydrogenase (GAPDH) as the internal reference gene.

4.13 Cell migration

L929 cells were seeded at a density of 1×10^6 cells/mL in a 6-well plate and cultured for 24 h. A scratch was created in the cell monolayer using a 20-μL pipette tip, followed by washing with PBS. The cells were treated with different hydrogel extracts, and images were captured using an optical microscope. Cell migration rates were calculated using the following equation (Eq. (4)):

$$\text{Cell migration rate}\ (\%) = \frac{S_0 - S_t}{S_0} \times 100\% \quad (4)$$

where S_0 and S_t represent the scratch areas before and after treatment, respectively.

4.14 RNA sequencing analysis

Cells from all groups (n = 3) were lysed in TRIzol reagent to extract total mRNA. RNA quality was assessed using a NanoDrop 2000 spectrophotometer and verified through RNase-free agarose gel

electrophoresis. After PCR amplification, RNA sequencing was performed using an Illumina sequencing platform (Genedenovo Biotechnology Co., Ltd., Guangzhou, China).

4.15 *In vitro* antimicrobial activity

S. aureus and *E. coli* were used as bacterial models. The antimicrobial efficacy of the hydrogel was evaluated via colony formation assays and live/dead bacterial staining. Bacterial morphology was observed using SEM and TEM. Specifically, bacterial suspensions (1×10^6 CFU/mL) of *S. aureus* and *E. coli* were added to 1 mL PBS containing Gel-GM hydrogel, incubated at 37 °C for 24 h, then diluted to 1×10^3 CFU/mL. Subsequently, 100 μL of each sample was spread onto tryptic soy broth (TSB) agar plates, incubated at 37 °C for another 24 h, and colonies were counted. Antimicrobial activities of the Gel-GM hydrogel and Blank (PBS) groups were compared.

4.16 Wound healing and histological analysis

Eight-week-old male C57BL/6J mice (Weitong Lihua Experimental Animal Center) were used to establish an infected wound model to assess therapeutic efficacy. Animal procedures were approved by the Institutional Animal Care and Use Committee of Peking University (DLASBD0391). Mice were anesthetized, and dorsal hair was completely removed. Subsequently, a full-thickness wound (6-mm diameter) was created using a skin biopsy punch, and 50 μL of *S. aureus* suspension (1×10^8 CFU/mL) was applied to induce infection [48, 49]. Wounds were treated with Blank (PBS), Gel hydrogel, and Gel-GM hydrogel, with dressings replaced every 3 days. Wounds were photographed on days 0, 3, 7, and 14, and skin tissues were harvested on days 7 and 14 for histological analysis. Tissue samples underwent H&E staining and Masson's trichrome staining. Epidermal regeneration and inflammatory responses were evaluated by IF staining of Ki67, α-SMA, CD86, and CD206. Vascularization and macrophage polarization were assessed via IHC staining of CD31, IL-10, and TNF-α.

4.17 Statistical analysis

Statistical analyses were conducted using GraphPad Prism 9 software (USA). Data are presented as mean ± SD. Statistical comparisons between multiple groups were performed using Student's *t*-test, one-way analysis of variance (ANOVA), or two-way ANOVA, followed by Tukey's multiple comparisons test. Significance is denoted as: $^*P < 0.05$, $^{**}P < 0.01$, $^{***}P < 0.001$, and $^{****}P < 0.0001$; ns indicates no statistical significance. Certain schematic diagrams were generated using BioRender (https://biorender.com/).

Electronic Supplementary Material: Supplementary material (synthesis and characterization of OSADA including UV–Vis, FTIR, and ^{1}H NMR; optimization of $NaIO_4$ crosslinking concentration and volume ratios; DPPH, ABTS, and ·OH radical scavenging assays; MD simulation setup and SASA analysis; adhesion test photographs on porcine skin and mouse organs; *in vitro* antibacterial evaluation with colony counting, LIVE/DEAD staining, and SEM/TEM) is available online at https://doi.org/10.26599/NR.2026.94908900.

Data availability

The data that support the findings of this study are available from the corresponding author upon reasonable request.

Acknowledgements

This work was supported by the National Key Research and Development Program of China (No. 2024YFA1210400, Y. L.), the National Natural Science Foundation of China (Nos. 82530030 and 82270954, Y. S. Z., and 82230030, Y. L.), Clinical Research Foundation of Peking University School and Hospital of Stomatology (Nos. PKUSS-2024CRF1002, CZPKUSS-2025CRF1002, and PKUSS-2023CRF1005, Y. S. Z.), the Non-profit Central Research Institute Fund of Chinese Academy of Medical Sciences (No. 2023-PT320-09, Y. S. Z.), Beijing Natural Science Foundation (No. L234017, Y. L.), Beijing Nova Program (No. 20240484655, Y. L.), Peking University Medicine plus X Pilot Program-Key Technologies R&D Project (No. 2024YXXLHGG004, Y. L.), and First-Class Discipline Team of Kunming Medical University (No. 2024XKTDTS08, Y. L.). We thank the National Center for Protein Sciences at Peking University in Beijing, China, for assistance with the confocal laser scanning microscopy (AXR, Nikon, Japan) and the digital pathology section scanning system (VS200, Olympus, Japan). We thank BioRender (https://biorender.com/) for providing the illustration platform for this study.

Declaration of competing interest

All the contributing authors report no conflict of interests in this work.

Author contribution statement

M. L.: Writing – review & editing, writing – original draft, methodology, data curation, conceptualization. H. Z.: Writing – review & editing, writing – original draft, methodology, data curation, conceptualization. Z. Q. W.: Software, methodology. M. Y.: validation, methodology. X. D. G.: Visualization, methodology. L. Y. C.: Software, methodology. X. J. C.: Project administration, methodology. Z. Y. W.: Software, methodology. L. F. F.: Project administration, methodology. L. W. L.: Supervision, conceptualization. Y. S. L.: Investigation, methodology, supervision. D. D. X.: Methodology, supervision. Y. L.: Writing – review & editing, supervision, funding acquisition, conceptualization. Y. S. Z.: Resources, supervision, funding acquisition, conceptualization.

Informed consent

Not applicable.

Ethics statement

All animal procedures were approved by the Animal Care and Use Committee of Peking University and conducted in accordance with ethical and welfare regulations (Ethical code: DLASBD0391).

Use of AI statement

None.

References

[1] Sharma, A.; Shankar, R.; Yadav, A. K.; Pratap, A.; Ansari, M. A.; Srivastava, V. Burden of chronic nonhealing wounds: An overview of the worldwide humanistic and economic burden to the healthcare system. *Int. J. Low. Extrem. Wounds* **2026**, *25*, 371–378.

[2] Guo, S.; Dipietro, L. A. Factors affecting wound healing. *J. Dent. Res.* **2010**, *89*, 219–229.
[3] Peña, O. A.; Martin, P. Cellular and molecular mechanisms of skin wound healing. *Nat. Rev. Mol. Cell Biol.* **2024**, *25*, 599–616.
[4] Uberoi, A.; McCready-Vangi, A.; Grice, E. A. The wound microbiota: Microbial mechanisms of impaired wound healing and infection. *Nat. Rev. Microbiol.* **2024**, *22*, 507–521.
[5] Long, L. Y.; Liu, W. Q.; Hu, C.; Yang, L.; Wang, Y. B. Construction of multifunctional wound dressings with their application in chronic wound treatment. *Biomater. Sci.* **2022**, *10*, 4058–4076.
[6] Lagoa, T.; Queiroga, M. C.; Martins, L. An overview of wound dressing materials. *Pharmaceuticals* **2024**, *17*, 1110.
[7] Nezhad-Mokhtari, P.; Hasany, M.; Kohestanian, M.; Dolatshahi-Pirouz, A.; Milani, M.; Mehrali, M. Recent advancements in bioadhesive self-healing hydrogels for effective chronic wound care. *Adv. Colloid Interface Sci.* **2024**, *334*, 103306.
[8] Liang, L.; Zhang, H.; Yao, F. L.; Li, J. J. Programmable tissue-adhesive hydrogels with temporal and spatial selectivity. *Chem. Soc. Rev.* **2025**, *54*, 12043–12079.
[9] Gong, Y.; Wang, P.; Cao, R.; Wu, J. Y. Z.; Ji, H. R.; Wang, M. S.; Hu, C.; Huang, P.; Wang, X. S. Exudate absorbing and antimicrobial hydrogel integrated with multifunctional curcumin-loaded magnesium polyphenol network for facilitating burn wound healing. *ACS Nano* **2023**, *17*, 22355–22370.
[10] Li, Y.; Sun, Z. H.; Chai, S. R.; Zhang, Z.; Li, Y.; Zhu, C. H.; Fan, D. D. Tissue-like soft dual-network hydrogel patch with instant/tunable adhesion and microenvironment modulation for infected wound healing. *ACS Nano* **2025**, *19*, 27714–27730.
[11] Jiang, Y. N.; Zhang, X.; Zhang, W.; Wang, M. H.; Yan, L. W.; Wang, K. F.; Han, L.; Lu, X. Infant skin friendly adhesive hydrogel patch activated at body temperature for bioelectronics securing and diabetic wound healing. *ACS Nano* **2022**, *16*, 8662–8676.
[12] Zhang, C.; Wu, B. H.; Zhou, Y. S.; Zhou, F.; Liu, W. M.; Wang, Z. K. Mussel-inspired hydrogels: From design principles to promising applications. *Chem. Soc. Rev.* **2020**, *49*, 3605–3637.
[13] Park, E.; Lee, J.; Huh, K. M.; Lee, S. H.; Lee, H. Toxicity-attenuated glycol chitosan adhesive inspired by mussel adhesion mechanisms. *Adv. Healthc. Mater.* **2019**, *8*, 1900275.
[14] Lv, C. L.; Li, L. L.; Jiao, Z. X.; Yan, H. H.; Wang, Z. L.; Wu, Z. X.; Guo, M.; Wang, Y.; Zhang, P. B. Improved hemostatic effects by Fe^{3+} modified biomimetic PLLA cotton-like mat via sodium alginate grafted with dopamine. *Bioact. Mater.* **2021**, *6*, 2346–2359.
[15] Xing, Q.; Zhen, L.; Zhou, X. L.; Zhong, S. T.; Li, F. X.; Li, J. Y.; Meng, R. Y.; Duan, P. P.; Luo, J.; Yang, J. J. Cohesion regulation of polyphenol cross‐linked hydrogel adhesives: From intrinsic cross‐link to designs of temporal responsiveness. *Adv. Funct. Mater.* **2025**, *35*, 2414294.
[16] Wan, Y. C.; Qiu, W. L.; Zhu, H.; Zhang, Q.; Zhu, S. P. Engineering cohesion and adhesion through dynamic bonds for advanced adhesive materials. *Can. J. Chem. Eng.* **2023**, *101*, 4941–4954.
[17] Song, R. J.; Wang, X.; Y. Johnson, M. ; Milne, C.; Lesniak-Podsiadlo, A.; Li, Y. H.; Lyu, J.; Li, Z. S.; Zhao, C. Y.; Yang, L. Z. et al. Enhanced strength for double network hydrogel adhesive through cohesion-adhesion balance. *Adv. Funct. Mater.* **2024**, *34*, 2313322
[18] Jung, H.; Kim, M. K.; Lee, J. Y.; Choi, S. W.; Kim, J. Adhesive hydrogel patch with enhanced strength and adhesiveness to skin for transdermal drug delivery. *Adv. Funct. Mater.* **2020**, *30*, 2004407.
[19] Gan, D. L.; Xing, W. S.; Jiang, L. L.; Fang, J.; Zhao, C. C.; Ren, F. Z.; Fang, L. M.; Wang, K. F.; Lu, X. Plant-inspired adhesive and tough hydrogel based on Ag-Lignin nanoparticles-triggered dynamic redox catechol chemistry. *Nat. Commun.* **2019**, *10*, 1487.
[20] da Silva, C. M.; Reis, R. L.; Correlo, V. M.; Jahno, V. D. The efficient role of sodium alginate-based biodegradable dressings for skin wound healing application: A systematic review. *J. Biomater. Sci. Polym. Ed.* **2024**, *35*, 397–414.
[21] Zhao, X. X.; Wang, W. Y.; Cheng, B.; Li, B. B.; Qiu, T.; Yan, L. S.; Wang, X. Y. Preparation of TEMPO-partially oxidized sodium alginate/SF scaffolds with degradation compatibility for skin defect repair. *Carbohydr. Polym.* **2025**, *357*, 123437.
[22] Zhao, J. Y.; Zhu, H. Q.; Xu, T. L.; Xu, S. Y.; Wang, Y. X.; Hou, Y. W.; Zhuo, M.; Du, K.; Su, Y. Y.; Han, X. et al. Self-healing oxidized dextran/sodium alginate hydrogel dressing with hemostatic activity speeds up wound healing in burn injuries. *ACS Appl. Mater. Interfaces* **2025**, *17*, 2940–2951.
[23] Bai, Z. X.; Dan, W. H.; Yu, G. F.; Wang, Y. J.; Chen, Y. N.; Huang, Y. P.; Yang, C. K.; Dan, N. H. Tough and tissue-adhesive polyacrylamide/collagen hydrogel with dopamine-grafted oxidized sodium alginate as crosslinker for cutaneous wound healing. *RSC Adv.* **2018**, *8*, 42123–42132.
[24] Hasani-Sadrabadi, M. M.; Sarrion, P.; Pouraghaei, S.; Chau, Y.; Ansari, S.; Li, S.; Aghaloo, T.; Moshaverinia, A. An engineered cell-laden adhesive hydrogel promotes craniofacial bone tissue regeneration in rats. *Sci. Transl. Med.* **2020**, *12*, eaay6853.
[25] Zhang, T.; Zhong, X. C.; Feng, Z. X.; Lin, X. Y.; Chen, C. Y.; Wang, X. W.; Guo, K.; Wang, Y.; Chen, J.; Du, Y. Z. et al. An active shrinkage and antioxidative hydrogel with biomimetic mechanics functions modulates inflammation and fibrosis to promote skin regeneration. *Bioact. Mater.* **2025**, *45*, 322–344.
[26] Huang, X. X.; Wang, J. J.; Wang, H. Q.; Ma, R.; Ling, Z. H.; Chen, K.; Xu, Z. C.; Ren, J. N.; Wu, X. W.; Zhang, Q. H. et al. Silver-catechol dynamic redox chemistry provides hydrogel dressings with sustained antioxidant and antibacterial activity for chronic wound care. *ACS Nano* **2025**, *19*, 22270–22290.
[27] Grosjean, M.; Girard, E.; Bethry, A.; Chagnon, G.; Garric, X.; Nottelet, B. Degradable bioadhesives based on star PEG-PLA hydrogels for soft tissue applications. *Biomacromolecules* **2023**, *24*, 4430–4443.
[28] Li, L. Y.; Liu, Z.; Qi, R. H. Molecular dynamics simulations in hydrogel research and its applications in energy utilization: A review. *Energy Rev.* **2024**, *3*, 100072.
[29] Wang, L.; Zhang, X. H.; Yang, K.; Fu, Y. V.; Xu, T. S.; Li, S. L.; Zhang, D. W.; Wang, L. N.; Lee, C. S. A novel double-crosslinking-double-network design for injectable hydrogels with enhanced tissue adhesion and antibacterial capability for wound treatment. *Adv. Funct. Mater.* **2020**, *30*, 1904156.
[30] Yu, L. S.; Liu, Z. D.; Tong, Z. R.; Ding, Y. H.; Qian, Z. F.; Wang, W. L.; Mao, Z. W.; Ding, Y. Sequential-crosslinking fibrin glue for rapid and reinforced hemostasis. *Adv. Sci.* **2024**, *11*, 2308171.
[31] Wang, Y. Y.; Wang, X. Y.; Liu, X. X.; Niu, C. Q.; Yu, G. T.; Hou, Y. J.; Hu, C.; Zhao, K.; Shi, J. Fabrication, characterization and potential application of biodegradable polydopamine-modified scaffolds based on natural macromolecules. *Int. J. Biol. Macromol.* **2023**, *253*, 126596.
[32] Shi, W. W.; Zhang, D. Q.; Han, L. Y.; Shao, W. T.; Liu, Q. M.; Song, B. Y.; Yan, G. Q.; Tang, R. P.; Yang, X. F. Supramolecular chitin-based hydrogels with self-adapting and fast-degradation properties for enhancing wound healing. *Carbohydr. Polym.* **2024**, *323*, 121374.
[33] Yuan, P. Y.; Deng, M.; Li, X. R.; Lu, X. T.; Yang, H.; Jin, R. H.; Wang, L.; Chen, M.; Bai, T.; Liu, T. et al. *Lactobacillus* extracellular vesicle-driven oxygen-releasing photothermal hydrogel reprograms macrophages and promotes angiogenesis to accelerate diabetic wound healing. *Bioact. Mater.* **2025**, *54*, 144–158.
[34] Wu, K. K.; Fu, M. M.; Zhao, Y. T.; Gerhard, E.; Li, Y.; Yang, J.; Guo, J. S. Anti-oxidant anti-inflammatory and antibacterial tannin-crosslinked citrate-based mussel-inspired bioadhesives facilitate scarless wound healing. *Bioact. Mater.* **2023**, *20*, 93–110.
[35] Seliktar, D. Designing cell-compatible hydrogels for biomedical applications. *Science* **2012**, *336*, 1124–1128.
[36] He, X.; Liu, X. Z.; Yang, J.; Du, H. B.; Chai, N. W.; Sha, Z.; Geng,

M. R.; Zhou, X. J.; He, C. L. Tannic acid-reinforced methacrylated chitosan/methacrylated silk fibroin hydrogels with multifunctionality for accelerating wound healing. *Carbohydr. Polym.* **2020**, *247*, 116689.

[37] Wu, K. K.; Wu, X. X.; Guo, J. S.; Jiao, Y. P.; Zhou, C. R. Facile polyphenol-europium assembly enabled functional poly($_L$-lactic acid) nanofiber mats with enhanced antioxidation and angiogenesis for accelerated wound healing. *Adv. Healthc. Mater.* **2021**, *10*, 2100793.

[38] Schutyser, E.; Struyf, S.; Van Damme, J. The CC chemokine CCL20 and its receptor CCR6. *Cytokine Growth Factor Rev.* **2003**, *14*, 409–426.

[39] Li, Z. J.; Burns, A. R.; Miller, S. B.; Smith, C. W. CCL20, γδ T cells, and IL-22 in corneal epithelial healing. *FASEB J.* **2011**, *25*, 2659–2668.

[40] Hattori, N.; Mochizuki, S.; Kishi, K.; Nakajima, T.; Takaishi, H.; D'Armiento, J.; Okada, Y. MMP-13 plays a role in keratinocyte migration, angiogenesis, and contraction in mouse skin wound healing. *Am. J. Pathol.* **2009**, *175*, 533–546.

[41] Wu, Y.; Wang, Y.; Zheng, C.; Hu, C.; Yang, L.; Kong, Q. Q.; Zhang, H.; Wang, Y. B. A versatile glycopeptide hydrogel promotes chronic refractory wound healing through bacterial elimination, sustained oxygenation, immunoregulation, and neovascularization. *Adv. Funct. Mater.* **2023**, *33*, 2305992.

[42] Epand, R. M.; Epand, R. F. Bacterial membrane lipids in the action of antimicrobial agents. *J. Pept. Sci.* **2011**, *17*, 298–305.

[43] Sun, Y.; Dong, W. B.; Sun, L.; Ma, L. J.; Shang, D. J. Insights into the membrane interaction mechanism and antibacterial properties of chensinin-1b. *Biomaterials* **2015**, *37*, 299–311.

[44] Cao, S.; Li, L.; Du, Y.; Gan, J. F.; Wang, J.; Wang, T.; Liu, Y.; Liu, W.; Zhou, Y. J.; Gao, X. et al. Porous gelatin microspheres for controlled drug delivery with high hemostatic efficacy. *Colloids Surf. B: Bioint.* **2021**, *207*, 112013.

[45] Lan, L.; Tian, F. R.; Zhuge, D. L.; Zhuge, Q. C.; Shen, B. X.; Jin, B. H.; Huang, J. P.; Wu, M. Z.; Fan, L. X.; Zhao, Y. Z. et al. Implantable porous gelatin microspheres sustained release of bFGF and improved its neuroprotective effect on rats after spinal cord injury. *PLoS One* **2017**, *12*, e0173814.

[46] Lozeau, L. D.; Grosha, J.; Smith, I. M.; Stewart, E. J.; Camesano, T. A.; Rolle, M. W. Alginate affects bioactivity of chimeric collagen-binding LL37 antimicrobial peptides adsorbed to collagen-alginate wound dressings. *ACS Biomater. Sci. Eng.* **2020**, *6*, 3398–3410.

[47] Nordström, R.; Browning, K. L.; Parra-Ortiz, E.; Damgaard, L. S. E.; Häffner, S. M.; Maestro, A.; Campbell, R. A.; Cooper, J. F. K.; Malmsten, M. Membrane interactions of antimicrobial peptide-loaded microgels. *J. Colloid Interface Sci.* **2020**, *562*, 322–332.

[48] Li, Y.; Yang, Z. F.; Sun, Q.; Xu, R. J.; Li, R. J.; Wu, D. C.; Huang, R. K.; Wang, F.; Li, Y. Biocompatible cryogel with good breathability, exudate management, antibacterial and immunomodulatory properties for infected diabetic wound healing. *Adv. Sci.* **2023**, *10*, 2304243.

[49] Zhao, X.; Wang, L. Y.; Tang, C. Y.; Zha, X. J.; Liu, Y.; Su, B. H.; Ke, K.; Bao, R. Y.; Yang, M. B.; Yang, W. Smart $Ti_3C_2T_x$ MXene fabric with fast humidity response and joule heating for healthcare and medical therapy applications. *ACS Nano* **2020**, *14*, 8793–8805.

This is an open access article under the terms of the Creative Commons Attribution 4.0 International License (CC BY 4.0, https://creativecommons.org/licenses/by/4.0/).

© The Author(s) 2026. Published by Tsinghua University Press.